Composition and Origin of the Volcanic Sedimentary Breccia Unit at the Carrapateena Iron-Oxide-Copper-Gold Deposit, SA

Thesis submitted in accordance with the requirements of the University of Adelaide for an Honours Degree in Geology/Geophysics

Dana Jayne Leslie

November 2020

THE UNIVERSITY
of ADELAIDE

COMPOSITION OF THE VOLCANIC SEDIMENTARY BRECCIA AT THE

CARRAPATEENA IRON-OXIDE-COPPER-GOLD DEPOSIT, SA

VOLCANIC SEDIMENTARY BRECCIA AT CARRAPATEENA

ABSTRACT

The Carrapateena Iron Oxide Copper Gold (IOCG) deposit is located on the eastern margin of the Gawler Craton. Economic Cu mineralisation is hosted by the Carrapateena Breccia Complex (CBC) which sits within in the Donington Granite. The Volcanic Sedimentary Breccia Unit (VSB) of unknown origin lies within the CBC and is considered to be uneconomically mineralised. Preliminary investigation suggests that the VSB was deposited after the main mineralisation event at Carrapateena, and therefore may provide important geological constraints on the age, evolution and preservation of the ore system.

This study focuses on six samples from the VSB. Multiple techniques were used to investigate the mineralogy and composition of the VSB, including; MAIA mapping, optical microscope petrography, SEM, SEM-CL and SEM-MLA.

The VSB can be described as a matrix supported sedimentary breccia/conglomerate with clasts of angular quartz, rounded volcanics, granite and lithics. The VSB is dominated by a fine chlorite with quartz and chlorite making up over 64% of the VSB by area.

In order to constrain the age of the VSB, in-situ U-Pb geochronology and trace element analysis was undertaken on zircon, monazite and rutile. The concordant U-Pb zircon analyses resulted in two populations of ages with modern day Pb loss trends. Zircons with higher Th/U correspond to a younger population with a weighted $^{207}Pb/^{206}Pb$ age of 1619 ± 10 Ma, correlating to St Peter Suite age. Zircons with lower U/Th ratios correspond to the age of the Donington Suite granite host rock at ca. 1855 Ma. Monazite from the non-mineralised samples were also shown to reflect the age of the host Donington suite granite. Monazites from the mineralised sample are interpreted as hydrothermal in origin, and have a range of ages from 1200 to 2100 Ma with a concentration around 1660 Ma, indicating the potential for multiple mineralisation or hydrothermal remobilisation event(s).

KEYWORDS

Sedimentary , Volcanic, Breccia, Conglomerate , IOCG, Carrapateena, Geochronology

CONTENTS

LIST OF FIGURES AND TABLES

Table of Figures

List of Tables

1. INTRODUCTION

The Carrapateena iron oxide copper-gold (IOCG) deposit is located on the eastern margin of the Gawler craton of South Australia. In 2019 it had a reported total mineral resource of 970 Mt at 0.5% copper, 0.2g/t gold and 3 g/t silver.

The Carrapateena iron oxide copper-gold (IOCG) deposit is hosted by the Carrapateena Breccia Complex (CBC) within the Donington suite granite (~1855 Ma; Jagodzinski, 2005) and contains significant volumes of rocks with a proposed sedimentary origin termed the Volcanic Sedimentary Breccia (VSB; Sawyer, 2014a). No comprehensive research has been completed on the sedimentary rocks in the CBC, and therefore their origin, depositional age, and relationship to the ore system are currently unknown.

This study aims to address the following research questions;

- What is the composition of the Volcanic Sedimentary Breccia?

- What is the age and origin of the Volcanic Sedimentary Breccia?

- What was the tectonic setting at the time of the formation of the Volcanic Sedimentary Breccia and the resultant brecciation?

- Can the Volcanic Sedimentary Breccia host ore and/or REE minerals? And if yes, does it contain the same ore an REE mineralogy as the main ore breccia?

The mineralogical and chemical composition of the VSB will be constrained by MAIA mapping, optical petrography and SEM-MLA. The age of the VSB will be determined

by the U-Pb dating and trace element analysis of zircon, monazite and rutile by LA-ICP-MS.

2. GEOLOGY

2.1 Regional and District Geology

The Gawler Craton is the host of South Australian IOCG deposits including Carrapateena, Prominent Hill and the world-scale Olympic Dam deposit (Figure 1; Curtis et al., 2018). The Gawler Craton developed as the result of two major phases of tectonic activity (Hand et al., 2007). The first stage took place during the late Archean where felsic and mafic magmas were present during basin development (2560-2500 Ma) followed by collisional deformation (2465-2410 Ma; Reid, 2019). The second stage of tectonic events took place during the middle to late Paleoproterozoic and early Mesoproterozoic (2000-1450 Ma) and included the development of the Gawler Range Volcanics and Hiltaba Suite Granitoids between 1595-1590 Ma and 1595-1575 Ma (Fanning et al., 2009; Jagodzinski et al., 2016) which have been proposed to be related to the development of mineralisation in the Gawler Craton (Skirrow, 2002). Following the two major periods of tectonism was the transition of an active arc regime to continental interior environment (Hand et al., 2007).

The Olympic copper-gold province stretches 600 km along the eastern boundary of the Gawler Craton in South Australia. The province was formed as the result of the Gawler Range Volcanics and Hiltiba suite intrusion events from 1595-1575 Ma. This event is

also believed to have formed the multiple structural controlled mesothermal deposits

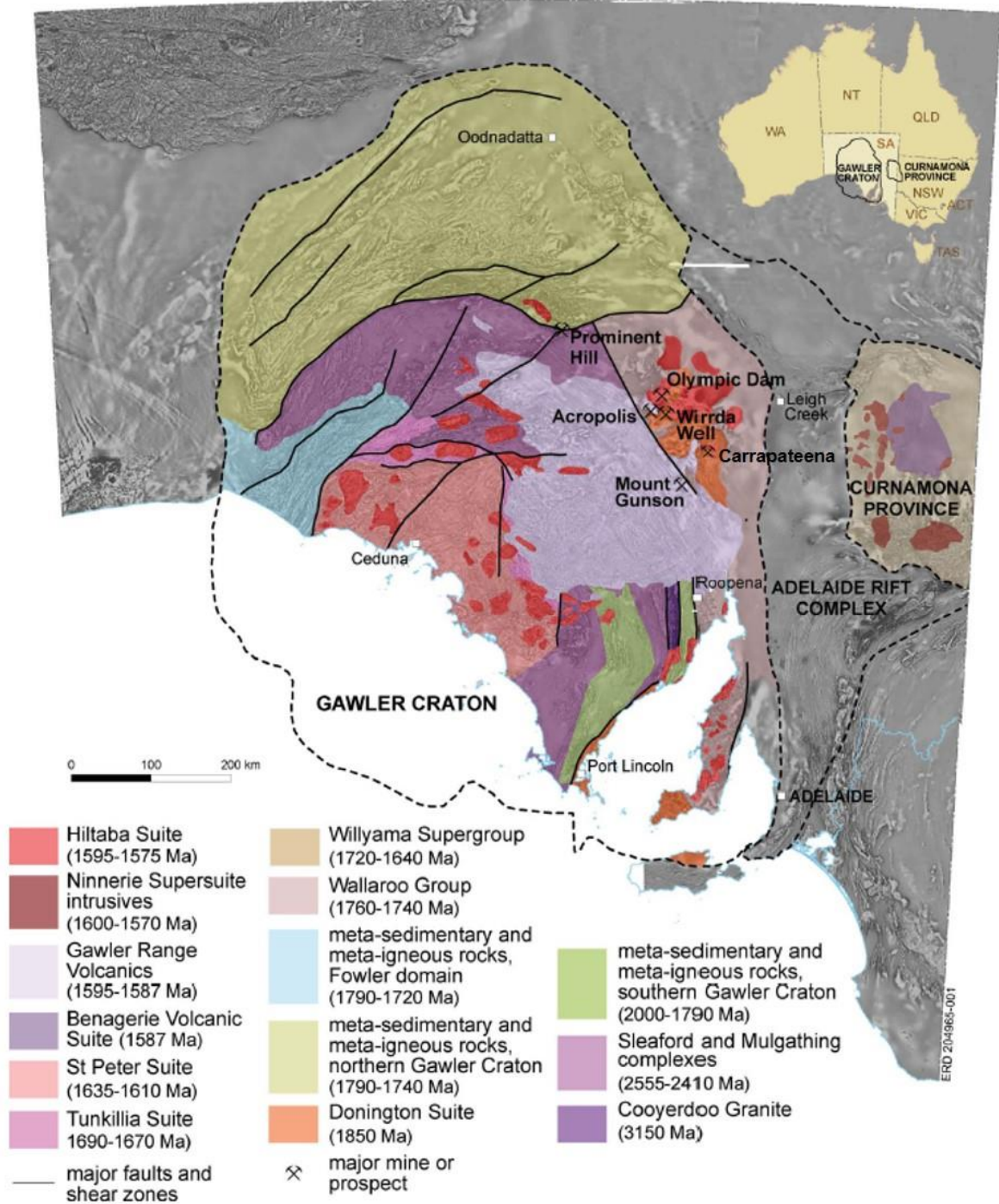which make up the Central Gawler Gold Province (Reid & Hand, 2012).

Figure 1 - Simplified solid geology of Gawler Craton and Curnamona Province (Curtis et al., 2018 adapted from Reid & Fabris, 2015) edited.

The Olympic Copper Gold province occurs above or adjacent to major crustal and lithospheric boundaries between the eastern Proterozoic terrane and central Archean terrane, making it subject to multiple stages of deformation (Reid, 2019).

There are three opposing tectonic models for the formation of IOCG's in the Olympic Copper Gold Province as proposed by Wade et al. 2006, Betts et al. 2009 and Skirrow et al. 2018 (Reid, 2019). Many models suggest mantle underplating or a mantle plume as the key driving mechanism (see Wade et al., 2019 and Daly et al., 1998).

Wade et al. (2006) modelled the Gawler Craton as distant from the arc and inferred back-arc extension linked to subduction to the north of the North Australian Craton underneath the Gawler Craton. Alternatively, Betts et al. (2019) & Skirrow et al. (2018) suggested a different relationship between subduction and magmatism with a switch in tectonic regime from compression to extension. Betts et al., (2006) suggested that the subduction zone and a mantle plume caused the tectonic regime to switch from compression to extension in the plate above. Skirrow et al. (2018) interpreted the Gawler Range Volcanics & Hiltiba Suite magmatism as a continental back-arc setting invoked occurring with delamination of the sub-continental lithospheric mantle underneath the Gawler Craton.

2.2 Local Geology

The local structures of Carrapateena were interpreted by Murphy et al. (2012) from magnetic, gravity and drill hole data. Five local rock packages were mapped consisting of the Donington Suite Granitoids, Wallaroo Group Sediments, Hiltaba Granitoids,

Galwer Range Volcanics and two major alteration styles characterized by hematite or

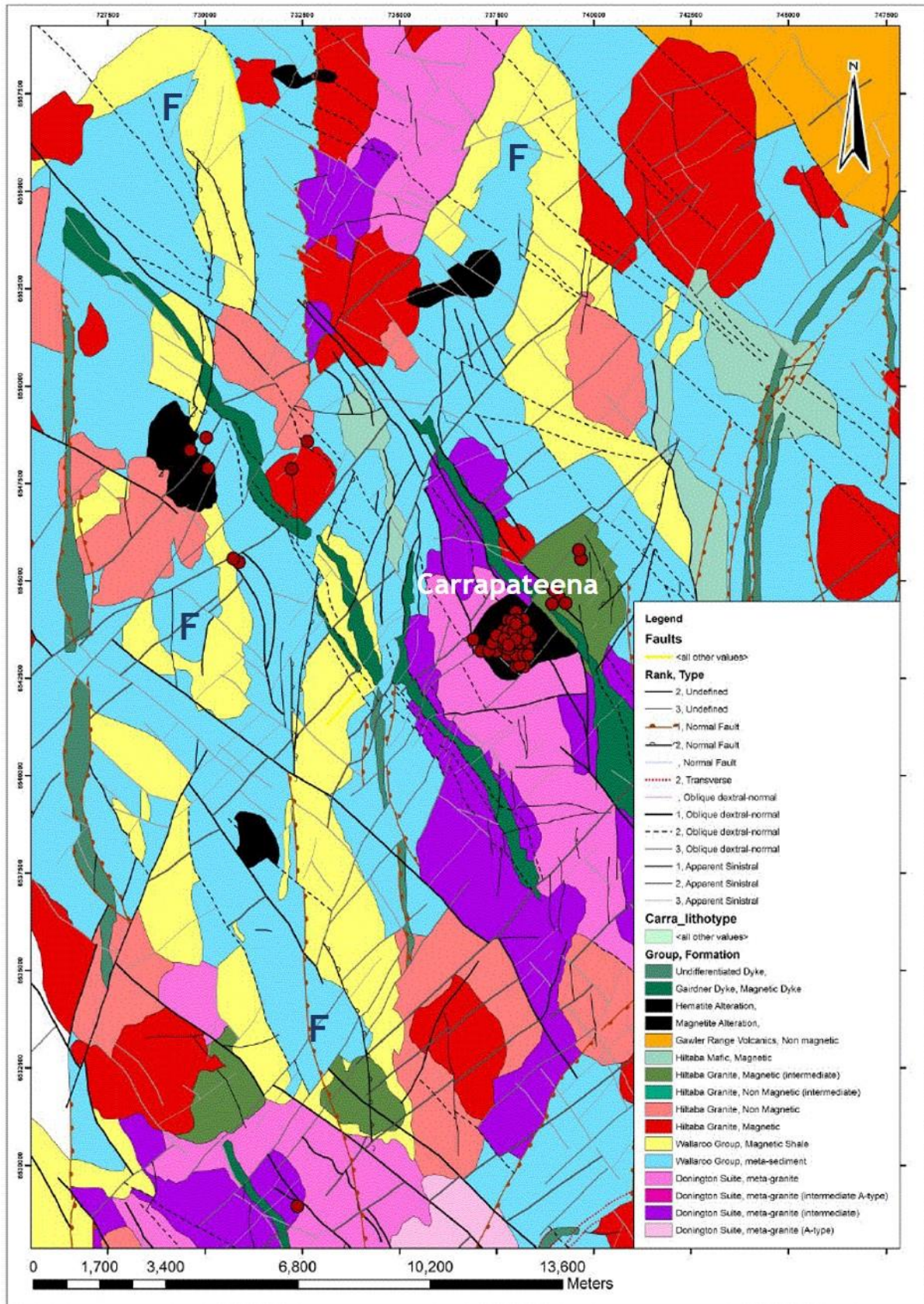magnetite dominant (Figure 2; Murphy et al., 2012).

Figure 2 - Geological interpretation showing the distribution of folds in the central and northern parts surrounding Carrapateena (Murphy et al., 2012) edited. Folds of the Wallaroo Group have

been denoted a blue F.

Four major fault sets were interpreted belonging to two different age groups of Hiltaba and Neoproterozoic related ages (Murphy et al., 2012). The Hiltaba aged dextral faults trend predominately NW and range from 1 to more than 10 km in strike (Murphy et al., 2012). The NE trending faults of Hiltaba age are sinistral and overprint the NW trending faults, implying they are younger in age (Murphy et al, 2012). The Neoproterozoic faults are mostly N-S normal faults that mostly dip towards the east. Faults to the east of Carrapateena, however dip towards the west, which has been interpreted as representing the edge of a graben (Murphy et al., 2012). The other Neoproterozoic fault sets are NE trending which have been interpreted as reactivation faults that control the distribution of the west dipping normal faults of the graben. The Carrapateena deposit sits on a fault intersection of major NW faults and large NE fault and coincident magnetic and gravity anomaly. Regional scale folds of the Wallaroo Group sediments are evident (Figure 2) and subsequently interpreted as north plunging with axial traces of NNW and NNE (Murphy et al., 2012). This folding has been interpreted by Murphy et al. (2012) as taking place during the Kimban Orogeny (1730-1690 Ma; Hand et al., 2007) because of the age constraint by overprinting later faults.

The Carrapateena deposit is hosted within a generally cylindrical breccia 'pipe' known as the Carrapateena Breccia Complex (CBC) of approximately 500 m in diameter and > 2000 m in depth, with the intensity of brecciation increasing towards the centre (Sawyer, 2014a). The CBC is located within the Donington Suite Granite (~1855 Ma; Jagodzinski, 2005) with ~480 m of overlaying Neoproterozoic (younger than 650 Ma) sedimentary rocks of the Stuart Shelf (Figure 3). Between the host rock and the

Neoproterozoic cover should lie unconformable units which occur locally of the eastern margin of the Gawler Craton. These units can include metasediments of the Wallaroo Group (1760-1740 Ma), the Gawler Range Volcanics (1595-1590 Ma) and Pandurra Formation (1440 Ma) (Reid, 2019). However, these units are not present and have been interpreted to have been eroded away prior to the deposition of the existing Neoproterozoic cover (e.g. Sawyer, 2014a) .

Below the overlying sedimentary successions six major rock types have been classified within the CBC by OZ Minerals including; granite (host rock) , hematite/granite breccias with copper sulphide and gold mineralisation, barren hematite breccias, chlorite/granite breccias, volcanic sedimentary breccia and dykes (mostly mafic and fewer felsic (Sawyer, 2014b).

Geology of Non-Granitic Rocks

The Neoproterozoic cover from the unconformity to surface consists of a basal conglomerate, Whyalla Sandstone with a dolomite member, Woomera Shale, Corraberra Sandstone and Arcoona Quartzite. As described above the breccia complex is composed of six Paleo-Mesoproterozoic basement groups. The hematite breccia hosts most of the copper mineralisation as chalcopyrite and bornite which is typically fine to medium grained and the barren hematite is often massive or vuggy in texture (Sawyer, 2014a). Dykes of intermediate to mafic in composition occur within Carrapateena and are observed as pre and syn brecciation of the complex.
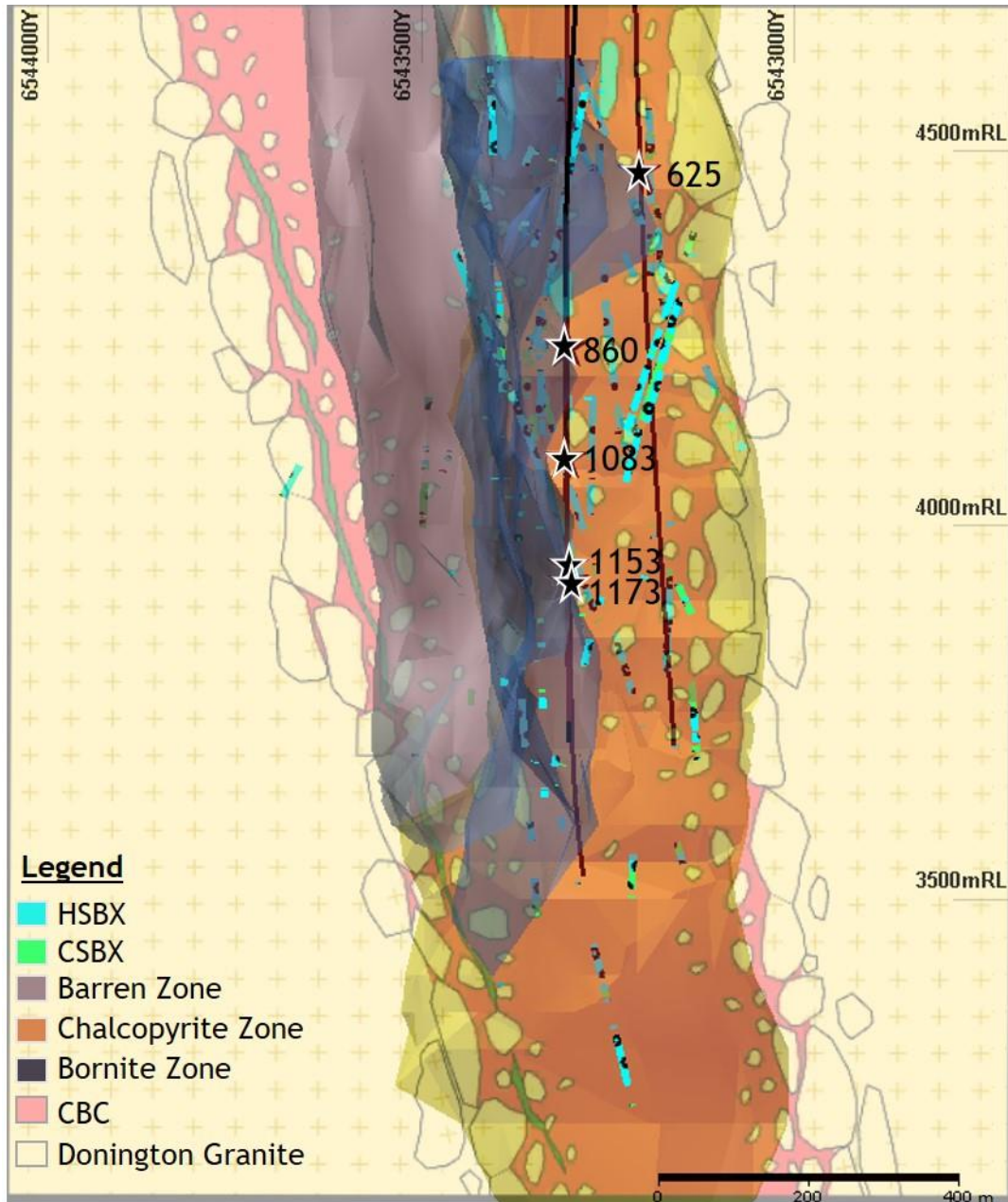
Figure 3 - Carrapateena Breccia Complex (CBC) looking east. Background cartoon image of CBC in Donington Suite Granite with overlapping micromine wireframe of the barren hematite, chalcopyrite and bornite zones with drill holes from this study and samples represented by stars. The VSB within the deposit is represented by hematite dominated volcanic sedimentary breccia (HSBX) and chlorite dominated volcanic sedimentary breccia (CSBX) lithology.

1.2 Geology of the Volcanic Sedimentary Breccia Unit (VSB)

The VSB unit has been described as a matrix supported polymictic breccia with clasts

ranging from sub-angular to sub-rounded and range from silt to pebble in size (Sawyer,

2014a). The clast themselves also vary in composition and include granite, quartz, mafic, felsic, clastic and pink volcanic clasts (Sawyer, 2014a). The matrix is fine and contain finely comminuted rock clasts and chlorite alteration. The VSB occurs as two compositional variations with hematite dominant (HSBX) and chlorite dominant (CSBX) alteration (Figure 5 and 6). The VSB Unit is present as vertical 'pods' of varying thickness which are located at different depths throughout the deposit (Mitchell Neumann, personal communication, July 2020). OZ Minerals undertook a program to relog the unit in 2013, but because of the difficulties of identification of the VSB units within a complex breccia system, it is suspected that the unit has not been identified in all locations where it has been drilled. The samples of VSB from this study range from 625 m depth to 1083 m (Figure 3). This unit has been logged up to a depth of 1960 m in drill hole DD12CAR091W and a thickness of 173 m in drill hole DD12CAR113.

Some VSB clasts have been visually identified as the Gawler Range Volcanics (GRV) which was determined by preliminary zircon dating (Bull and Meffre, 2012, 2013), petrographic description and occurrence of the GRV outcropping to the north and west of the deposit. There are currently two explanations as to how this unit was emplaced. (1) Sawyer (2014), suggested an analogy of Laughton (2004) where the VSB formed as a result of gravitational collapse of lava flows deposited in a low lying area as a result of the Carrapateena breccia system reaching the paleo-surface. (2) Taylor (2014) suggested that a narrow 'pipe' shaped void space could have been created by phaneritic eruptions and subsequentially filled from the surface with the observed GRV-derived clasts.

The VSB unit is of unknown origin and age, is observed to be disrupted by brecciation and hematite alteration typical of the ore zones (Sawyer, 2014a). Copper sulphides (chalcopyrite and bornite), are present in non-economic quantities as alteration and veins, indicating that the VSB must have been present in the CBC prior to and during ore forming or remobilisation events.
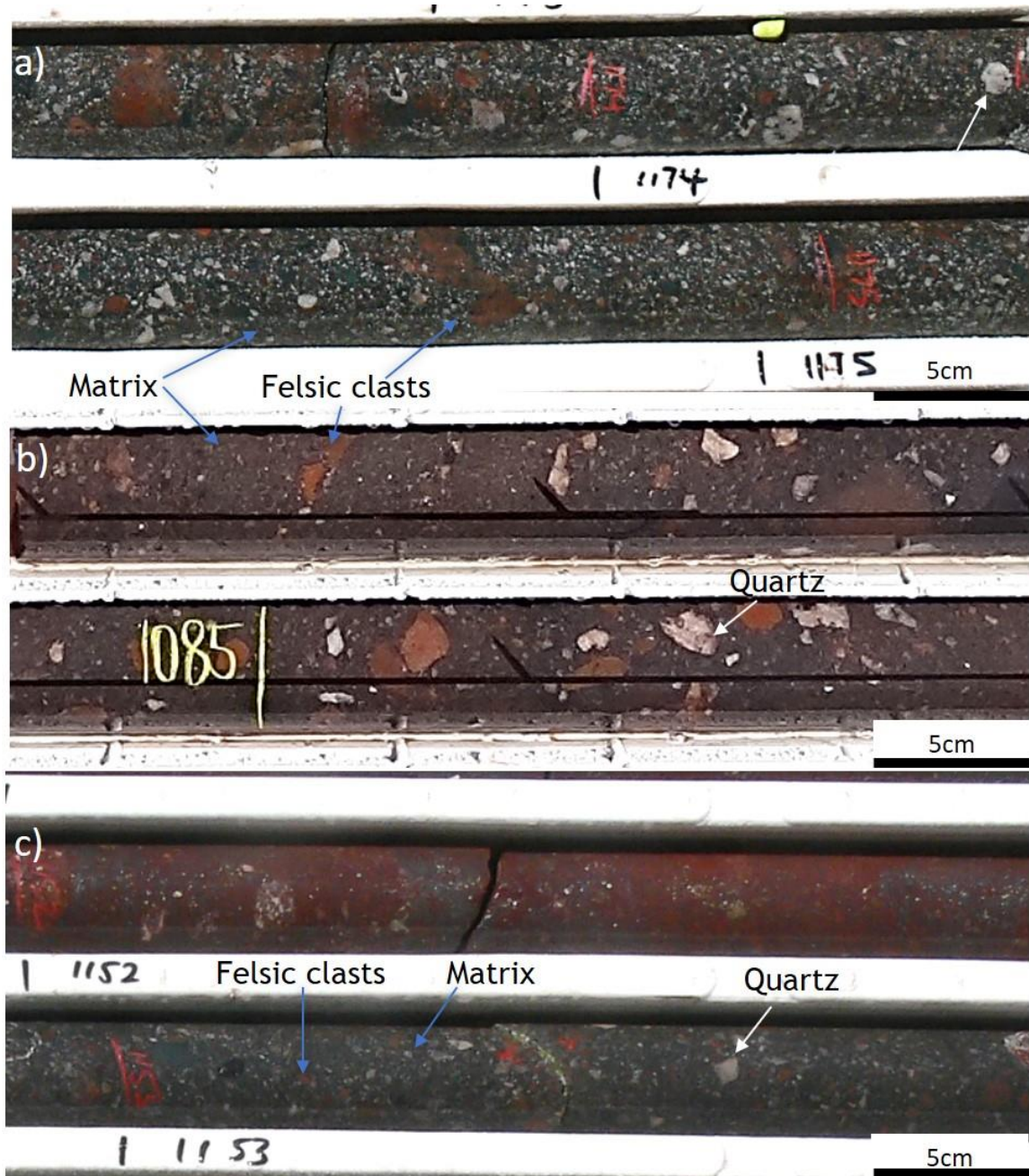
Figure 4 - A typical section of core representing the VSB unit. (a) CSBX sample 1173, CAR050 (b) CSBX sample 1083 from CAR083, (c) HSBX sample 1153, CAR050.

3. METHODS

3.1 Sample Selection

Core samples from OZ Minerals drill hole CAR083, which intercept the VSB unit were

obtained and used in this study. Moreover, a historical collection of Carrapateena thin

sections with known locations were also used in this study. Core sample CAR083

(Figure 5b) was made into three thin sections, with four historical thin sections from

CAR050 (Figure 5a and 5c) and CAR055 also selected for further analysis. A summary

of these samples in included in Table 1.

Table 1 - Petrological Sample Summary

Sample name	Drill core	Depth (m)	Lithology	Description
625	CAR055	625	HSBX	• Shallowest sample of study • Sericite altered
860	CAR050	860	GRAN?	• Previously identified as CSBX until drill core inspection
1153	CAR050	1153	HSBX	• Mineralised with chalcopyrite and bornite
1173	CAR050	1173	CSBX	• Contains large pink volcanic clast

1083 A, B and C	DD12CAR083	1083	CSBX	• Samples A and B mineralised with chalcopyrite • Sample C is not mineralised

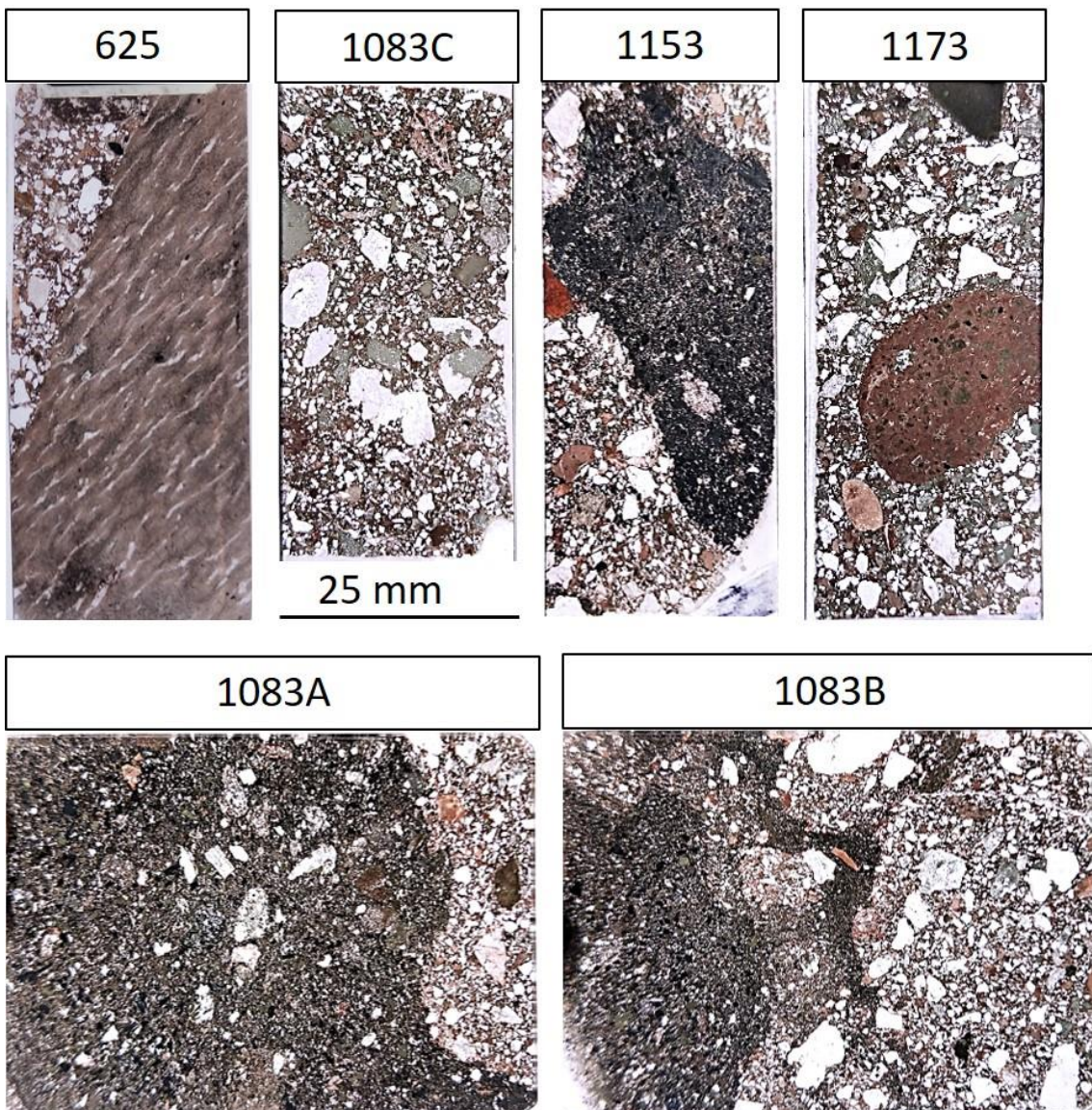**Figure 5 - VSB Thin Sections of this study, (Top Row, left to right); 625, 1083C, 1153 and 1173, (Bottom Row, left to right); 1083 A and 1083B**

3.2 MAIA Mapping

The CSIRO MAIA mapper is a non-invasive imaging technique that analyses the distribution of individual elements at the micron scale. The mapper is a X-Ray fluorescence (XRF) mapping system that targets up to 80M pixels over a 500 x150 mm² area (Ryan et al., 2018). The core sample of drill hole DD12CAR083 at 1083 m depth was sent to CIRSO MAIA mapping for a full suite of elements.

3.3 Petrography

Petrography was completed at Adelaide University using an Olympus BX51 System with an attachable DP21 microscope digital camera on polished thin sections 30 µm thick. Optical microscopes were used to complete petrography reports of the samples and identify areas of interest.

3.4 Scanning Electron Microscope (SEM) and Mineral Liberation Analysis (MLA)

All samples were analysed using the Quanta 600 Scanning Electron Microscope (SEM) at Adelaide Microscopy. The backscatter electron mode (BSE) was used to identify and take images of individual grains and textural relationships including intergrowths, inclusions and zonation. The silicon drift detector and X-ray energy dispersive detector (SDD EDS) was used to gain the semi-qualitative elemental composition to aid the different mineral phases. The two imaging modes used include electrode backscatter maps (EBS) and cathodoluminescence (CL) images with the parameters outlined in Appendix B.

The MLA was used to produce modal mineral maps and mineral associations of the VSB in the samples. A mineral list of 24 different mineral spectra were identified from the samples and used for classification. The classified images ranged from 3% to 12% of unidentified grains and was processed to under 2% as an accepted industry standard (Aofie McFadden, personal communication, June 2020) with the exception of the sample 625. Sample 625 was processed until the quality of the image was compromised by grain size. The resultant modal minerology of the samples has been displayed in Figure 8c with the associated data is included in Appendix B. The mineral associations in this paper relate to what minerals occur in contact with the grain boundary of the selected mineral calculated by the processing of the MLA maps.

The FEI Quanta 450 FEG Environmental Scanning Electron Microscope (ESEM) at Adelaide Microscopy was also used to observe mineral textures and relationships.

3.5 U-Pb Geochronology

The LA-ICP-MS was used to obtain quantitative compositional data of selected grains. The grains were selected from areas of interest from previous observations from SEM, MLA, MAIA mapping and petrography. The LA-ICP-MS uses a RESOlution LR 193nm Excimer laser system coupled to an Agilent 7900x ICP-Quadrupole Mass Spectrometer to provide the analysis of more than 25 elements as major elements and minor trace elements and isotopes. The settings used during this analysis are outlined in Appendix C.

The LA-ICP-MS was used to date zircon, rutile and monazite grains within the VSB. This was achieved by obtaining uranium and lead isotope data. The parameters of acquisition are listed in Appendix C.

3.5.1 DATA REDUCTIONS, STANDARDS AND ACCURACY

The LA-ICP-MS data was reduced using LADR software (Norris Scientific) (Norris & Danyushevsky, 2018) at Adelaide Microscopy. NIST 610 was used as a primary standard for all trace elements. The trace elements with the exception of Hg, were normalised to assume stoichiometric mineral compositions of zircon, monazite and rutile. GJ, MAdel and R10 standards for zircon, monazite and rutile respectively were used as primary standards for $^{207}Pb/^{206}Pb$, $^{206}Pb/^{238}U$, $^{207}Pb/^{235}U$. These primary standards were used for calibration to correct mass bias and elemental fractionation of U-Pb ratios. The primary standards were analysed frequently (approximately 30 min) to correct for instrument drift. The secondary standards (Appendix C) were used to monitor accuracy including two secondary standards for zircon (Pleisovince & 91500) and monazite (222 & Ambat) and one standard for rutile (R19). Normal isotopic abundances were assumed for ^{204}Hg measured from ^{202}Hg as to correct for potential interference with ^{204}Pb.

The zircon, rutile and monazite standards all produced ages that agree with the referenced values indicating the LA-ICP-MS data produced for this study is of high accuracy (Appendix C). The geochronological data for zircon, monazite and rutile was plotted using Isoplotr (Vermeesch, 2018).

4. OBSERVATIONS AND RESULTS

4.1 Minerology and Composition of the VSB

4.1.1 MAIA Mapper

MAIA mapper image data displays the relative abundances of selected elements from sample 1083 A, B and C. This data was used to interpret general mineral relationships of the VSB to assist MLA and LA-ICP-MS data collection. The general relationships observed relate to the areas of mineralisation and of the VSB (rock slab) as pictured in Figure 6a. The central mineralised vein contains most of the copper sulphide mineralisation and grey hematite (Figures 6a, 6b and 6c). Mineralisation is mainly absent within the VSB fragments incorporated in the breccia. As also evident in Figure 6b, are small copper sulphide occurrences within the VSB area of the rock. Other observations from the MAIA mapper data distinguished is the presence of Ce, Y, Zr in both the mineralisation and VSB (Figure 6d).
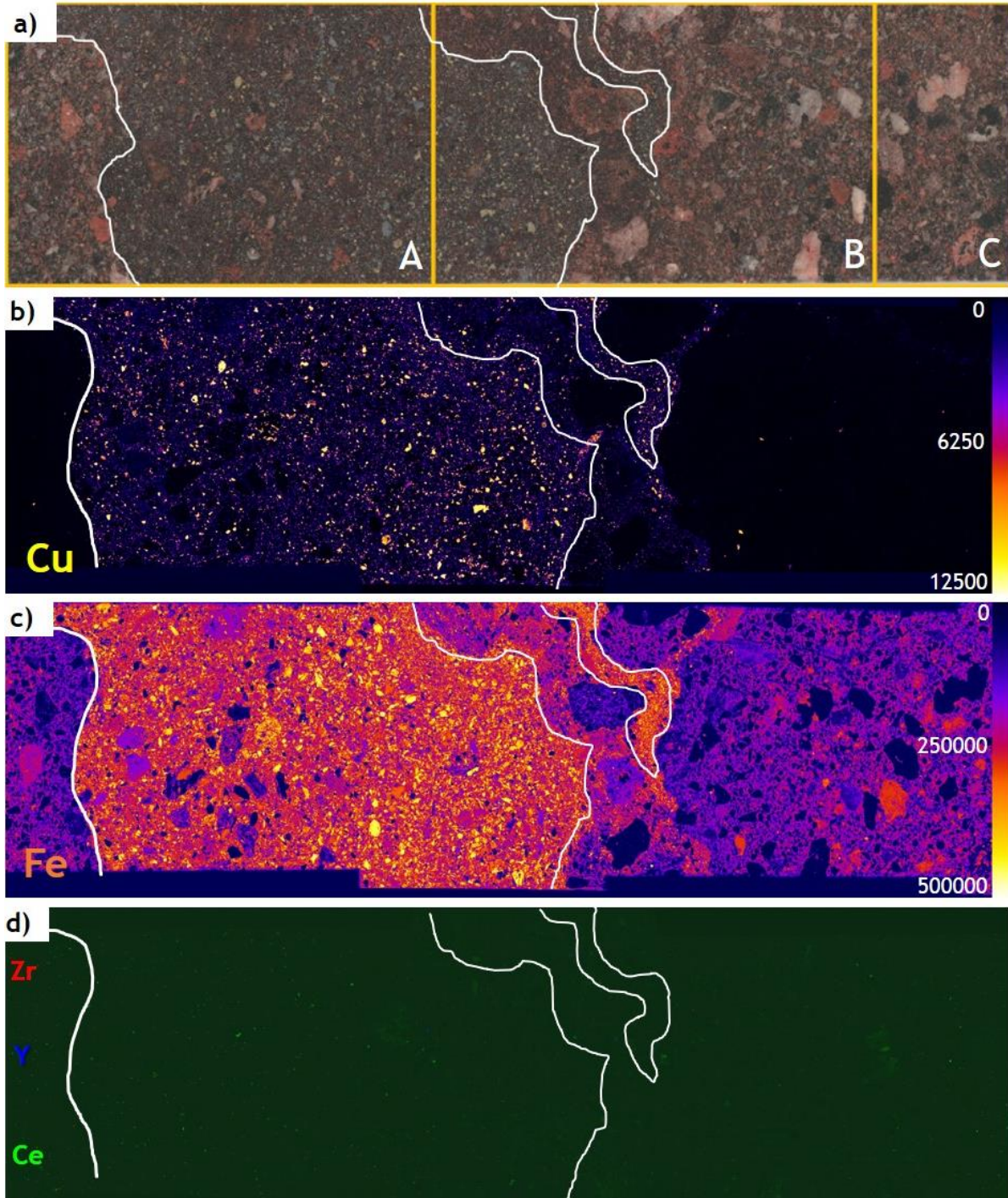
Figure 6 (a) Samples 1083A, B and C with white lines denoting areas of mineralisation in the centre and small veinlet with VSB unit on either side of mineralisation, Samples 1083A, B and C as mapped by the MAIA Mapper (b) Coloured by copper content in ppm, (c) C oloured by iron content in ppm, (d) Composite of Ce, Y and Zr content corresponding to green, blue and red respectively.

4.1.2 Optical Petrology of the VSB

The six VSB samples were analysed under reflected and transmitted light on the optical microscope at the University of Adelaide (Table 1). A full petrographic description of each sample can be found in Appendix A.

Sample 625 is representative of HSBX and consists of a weakly hematite altered matrix with sericite-dominant alteration throughout and selective clasts have been sericite altered. This sample contains a large ex-volcanic clast of a 10 cm diameter as observed in Figure 7a, which has been subject to stress and has been subsequently sheared before its inclusion within the VSB. The clast contains quartz foliations and sericite altered ex-feldspar phenocrysts. The groundmass of the clast is microcrystalline in texture and has been subject to sericite alteration. The remainder of the sample is composed of a breccia/conglomerate of angular quartz, sub-rounded lithic and granite clasts in a sericite/hematite altered matrix (Figure 7b). Minor disseminated hematite and chalcopyrite grains are observed in both the large volcanic clast and breccia/conglomerate area of the thin section. No chlorite was observed in the matrix.

Sample 860 is a granite breccia which was previously mis-logged by Teck as CSBX in the earlier days at Carrapateena. In this sample no felsic or pink volcanic clasts are observed and different grain sizes are present with a fine grained layer separating the larger grained areas of the thin section. The fine grained (5-30 microns in diameter) layer consists of very-fine milled grains of granite and hematite. This sample is weakly mineralised with chalcopyrite occurring as a smaller grain size (approximately 10 microns) but is higher in abundance within the fine-grained horizon.

24

Sample 1153 is a mineralised and hematite dominant VSB. Mineralisation is disseminated and present as bornite, chalcopyrite and occurs with pyrite clasts within the matrix (Figures 7e). Late stage chlorite veins carry chalcopyrite and other minor chalcopyrite veins are present in this thin section (Figure 7f). Other clasts in the conglomerate include volcanics (felsic and mafic variations), granite and angular clasts of quartz.

Sample 1173 is a hematite dominant conglomerate sample with no copper mineralisation. A rounded pink volcanic clast (2 x 3 cm size) is located within the chlorite altered matrix. This clast has mafic, ex-feldspars and quartz phenocrysts with micron sized magnetite (Figure 7g). The clast is hematite altered and has a glassy groundmass texture with altered shards and has been described as a rhyolite from a porphyry volcanic (Pontifex, 2012). Other clasts are predominantly angular quartz but includes lithic, granite, mafic and felsic volcanic clasts (Figure 7h).
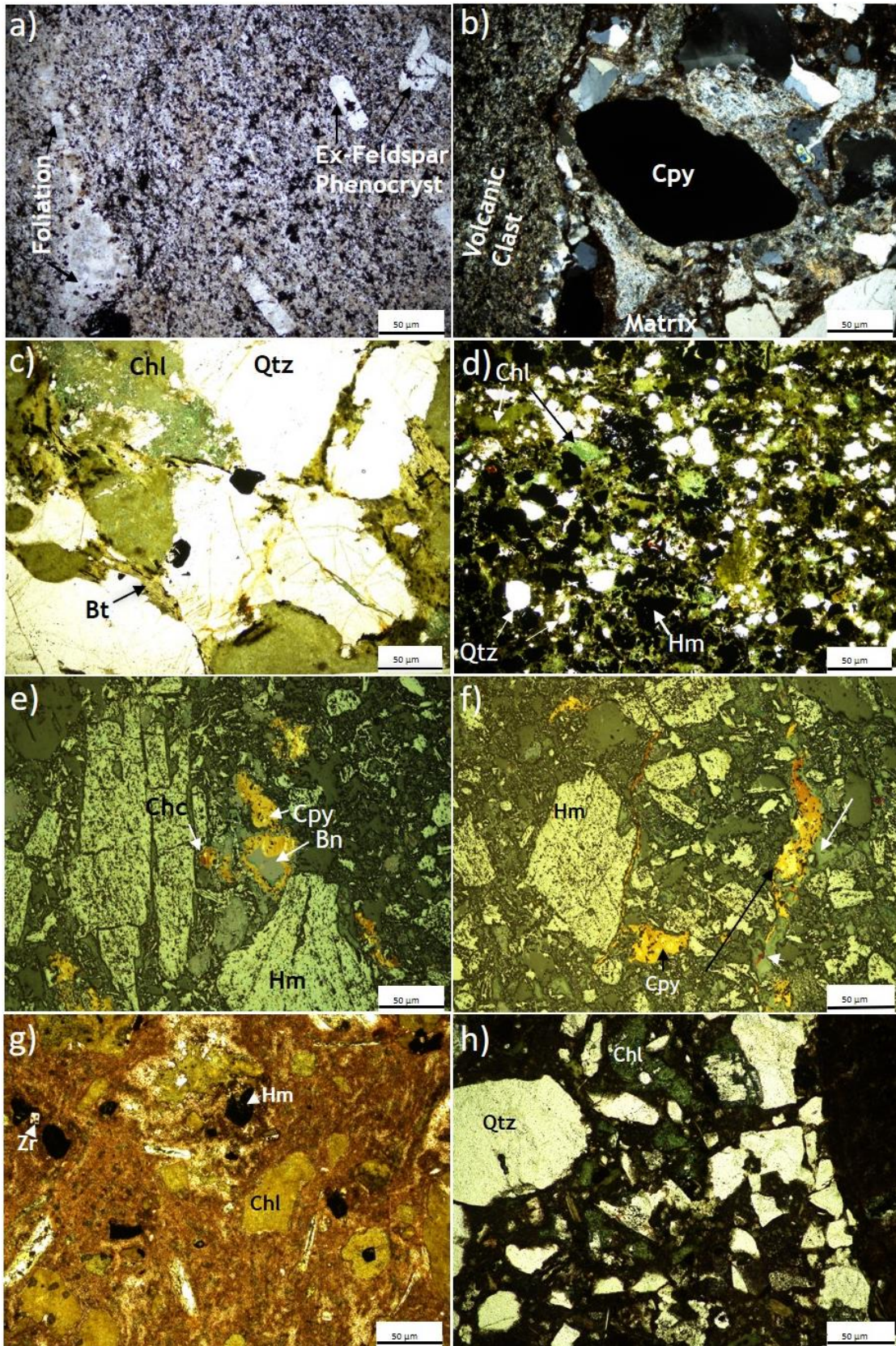
Figure 7 (a) Volcanic grain of sample 625 with sericite ex-feldspar clasts and a quartz foliation (TL), (b) Edge of volcanic grain and conglomerate of sample 625 (PL), (c) Granite clast of sample

860 consisting of course grained chlorite and quartz (TL), (d) Fine grained are area of sample 860 with hematite, quartz and chlorite clasts (TL), (e) Bornite rimmed by chalcopyrite in mineralised part of sample 1153 (RL), (f) Chalcopyrite and late chlorite veins in mineralised part of sample 1153 (RL), (g) Hematite stained volcanic clast of sample 1173 (TL), (h) Conglomerate area of sample 1173 consisting of angular quartz clasts and a fine chlorite matrix (TL). Qtz = Quartz, Cpy = Chlacopyrite, Chl = Chlorite, Bt = Biotite, Hm = Hematite, Bn = Bornite, Chc = Chalcanthite, TL = transmitted light, PL = polarised light, RL = reflected light.

Samples A, B and C from CAR083 at 1083 m depth represent a mineralised section of VSB which has been brecciated and subsequently cut by a vein carrying hematite (steele hematite) and hematite alteration (earthy hematite) (Figure 8c). Samples A and B have been brecciated and infilled by hematite alteration and subsequent mineralisation with the sulphides chalcopyrite and pyrite (Figure 8c). The clast within the mineralised sections consist of mainly angular quartz grains and lithic clasts from the conglomerate/breccia and hematite with minor occurrences of other clasts such as smaller comminuted rounded pink volcanic, mafic and other felsic grains (Figures 8a, 8b and 8d). Metasedimentary grains were also observed (Figure 8e) with a clast larger than 300 µm in size observed in sample 1083A (Figure 8f). The breccia/conglomerate is matrix supported and consists of chlorite and finer comminuted clasts.

In all samples the VSB is matrix supported and has polymictic grains. The matrix consists of fine chlorite and/or hematite and finer comminuted grains of the conglomerate/breccia. The clasts consist of mainly volcanic (felsic and ex-mafic), granite and lithic clasts which varied of size and concentration between samples. The angular quartz varies from 30-45% area and 3 µm to a 3 cm in size. The volcanic clasts within the VSB matrix have a range of textures and are often rounded fragments of mafic or felsic origins. Course grained chlorite of smooth appearance that when compared to the fine chlorite matrix has been interpreted as ex-mafic clasts (Figure 8f).

27

The interpreted felsic clasts contain mostly hematite stained quartz with inclusions of ex-feldspars which have been altered to chlorite that hold volcanic textures (Figure 7g and 8a). The lithic clasts consist of many different sizes, textures and compositions of quartz, chlorite and in some cases biotite or muscovite (Figure 8d). Course grained quartz and chlorite with minor iron oxides occurrences have been interpreted as chlorite altered granite (Figure 7c). Minor metasedimentary grains were also observed in samples 1083A and 1083C consisting of quartz and muscovite with muscovite defining foliation (Figure 8d and e).
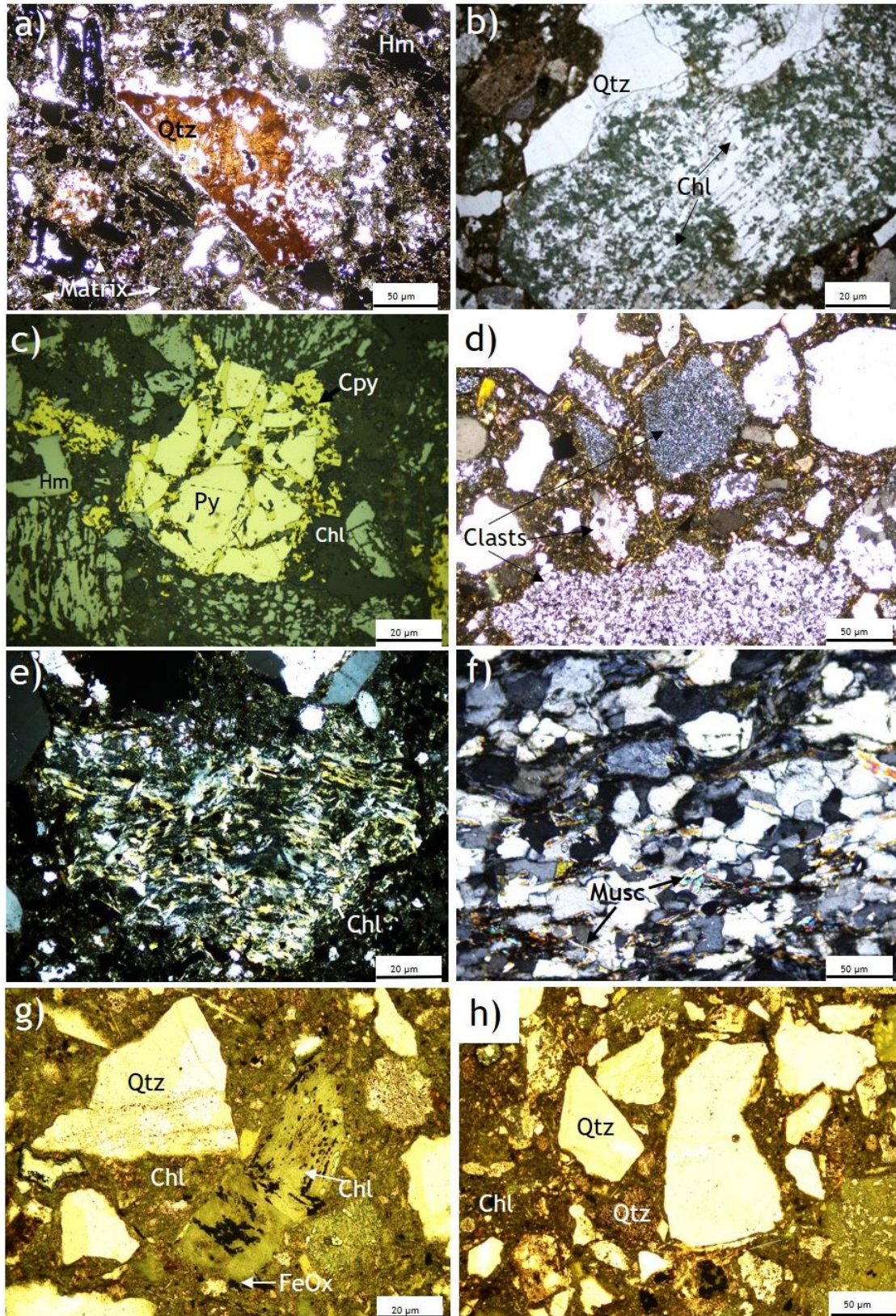
Figure 8 (a) Large felsic grain in mineralised area of sample 1083A (TL), (b) Granite/Gneiss of quartz and chlorite from sample 1083B (TL), (c) Pyrite grains surrounded by chalcopyrite in mineralised part of sample 1083B (RL), (d) Various clasts of conglomerate in fine chlorite matrix with minor biotite occurrences of sample 1083C (TL), (e) Metasediment clast of sample 1083B (PL), (f) Metasediment clast of quartz and muscovite defining the fabric of sample 1083A (PL), (g)

Chlorite clast with iron oxides possibly of ex-mafic clast (TL), (h) Angular quartz clasts within typical CSBX (TL). Qtz = Quartz, Cpy = Chlacopyrite, Chl = Chlorite, Bt = Biotite, Hm = Hematite, Py = Pyrite, FeOx = Iron Oxide, Musc = Muscovite, TL = transmitted light, PL = polarised light, RL = reflected light.

4.1.3 SEM-MLA mapping of the VSB
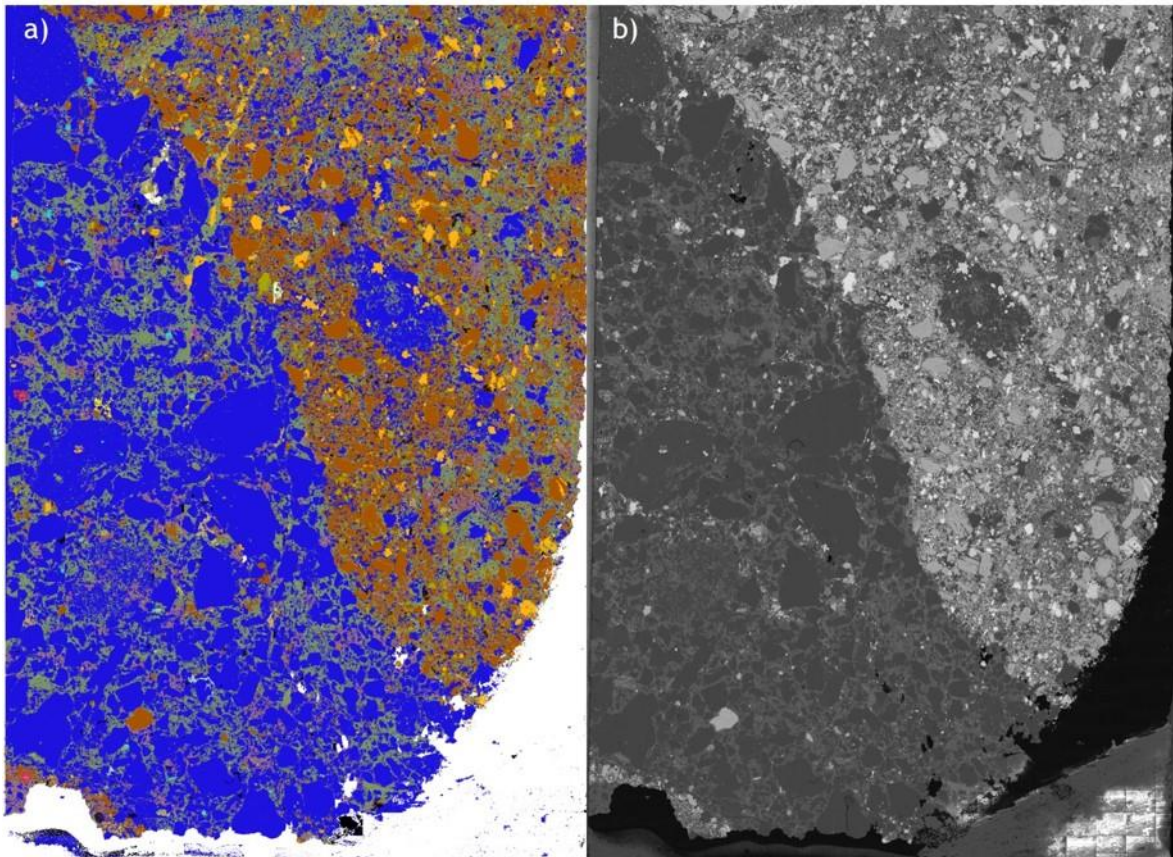
c) Modal Mineralogy (Area %)

Figure 9 (a) MLA processed image of sample 1153, (b) SEM scan in BSE mode of sample 1553, (c) Modal mineralogy of all samples by area %.
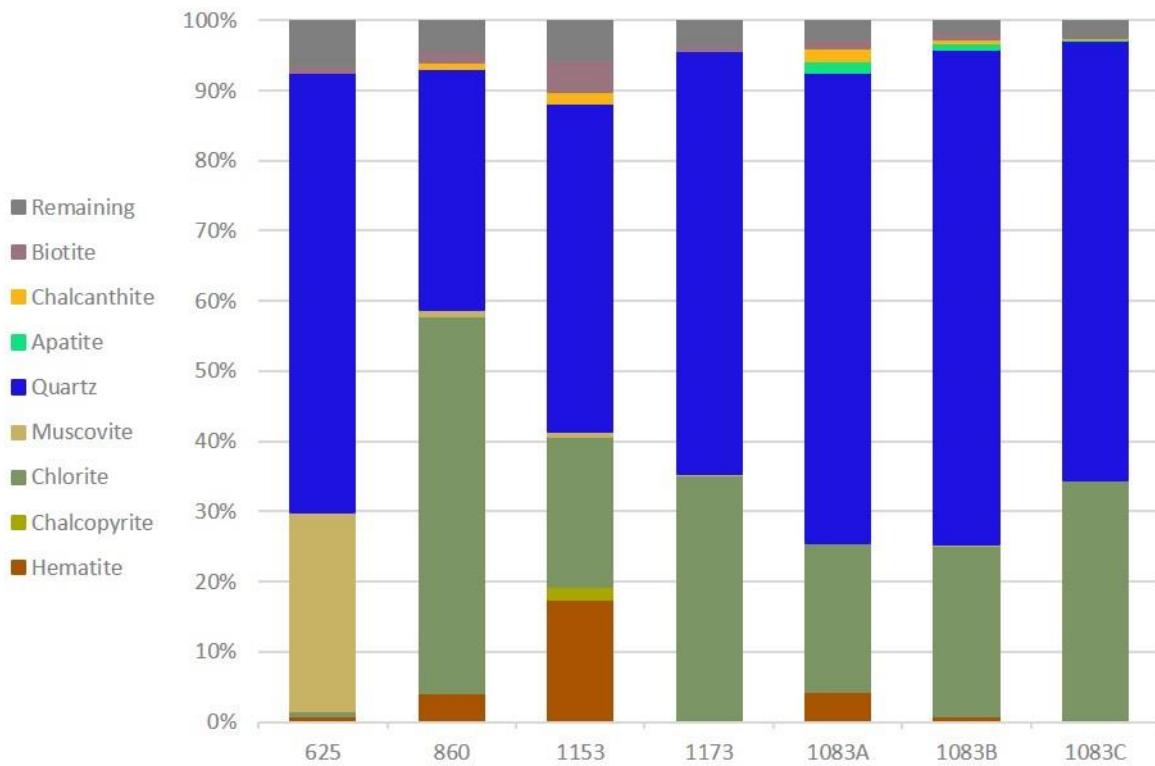
The SEM-MLA results agree with the petrographic observations with main concentrations by area of 1-35% (1-39 wt%) chlorite, 34-71% (32-69 wt%) quartz, 0-18% (0-30 wt%) hematite (Figure 9a and c). The samples with hematite alteration also have the highest content of sulphide minerals; bornite, pyrite, chalcopyrite and chalcanthite (Figures 7e, 7f and 8c). Additional minerals found with the SEM include; barite, a REE aluminate, monazite, galena, calcite, hessite, brannerite, xenotime, apatite, ilmenite and a Ce-silicate (Appendix B).

The REE bearing minerals of REE aluminate, Ce-silicate and xenotime have mineral associations with chlorite and quartz of over 65%. The Ce-silicate is associated with over 60% with quartz (22.4% chlorite) where the REE aluminate and xenotime occurs with over 62% and 42% with chlorite (16% and 26% quartz). The ore minerals are located mostly with hematite including chalcopyrite ($CuFeS_2$), chalcanthite ($CuSO_4 \cdot 5H_2O$) (after bornite and chalcopyrite) and hessite (Ag_2Te) at 53.6%, 25.3% and 23.5% association respectfully.

The HSBX (hematite dominated VSB) however has a similar copper content to HMX at approximately 11,000 ppm. Compared to the main hematite breccia which host the ore (HMX), the CSBX (Chlorite dominated VSB) has lower mean copper content at approximately 5700 ppm but is found to have much higher values than the granite (GRAN) and barren zone (BHMX) (Figure 10) at 350 and 400 ppm respectively. The REE content of the HSBX, HMX and BHMX are similar occurring above 10,000 ppm

with the CSBX having a slightly lower content at 9100 ppm but is still enriched in REE

compared to GRAN at 4000 ppm (Figure 10).
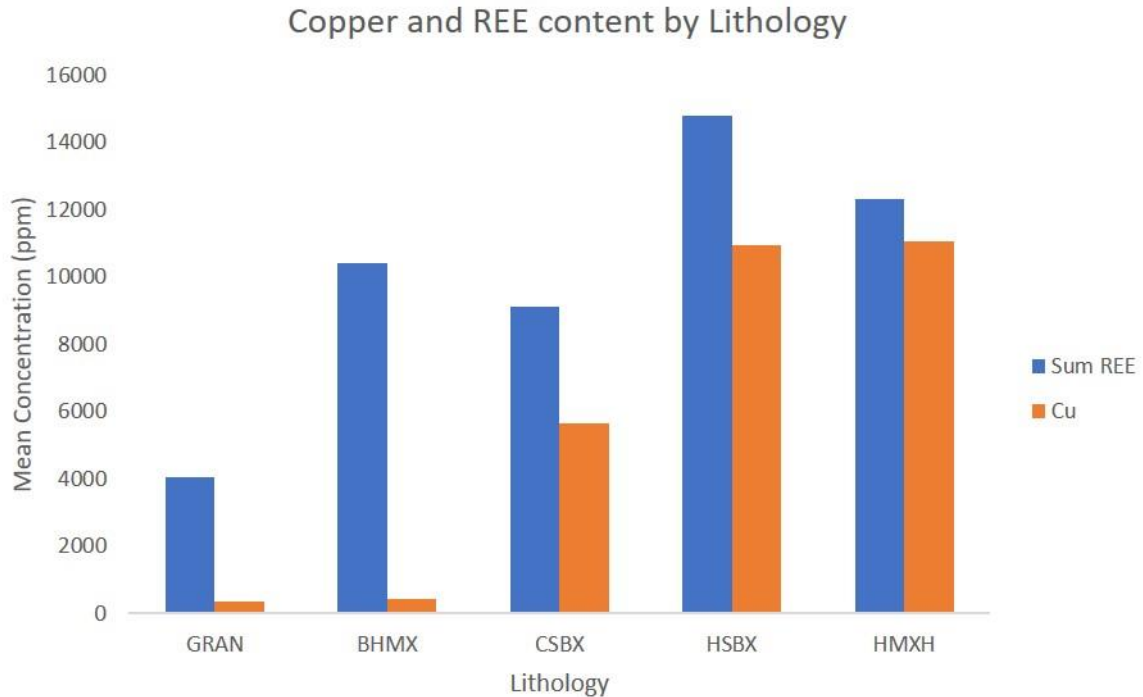
Figure 10 - Mean Copper and REE content of Granite (GRAN), Baren Hematite Breccia (BHMX), Chlorite dominated VSB (CSBX), Hematite dominated VSB (HSBX) and Hematite Breccia (HMXH).

4.2 ZIRCON GEOCHEMISTRY AND GEOCHRONOLOGY

4.3.1 Zircon Mineralogy

The zircons shapes and sizes vary (10-120 µm) and are mostly carried in the fine

chlorite matrix but also occur in the mineralised areas of samples 1083A, 1083B and

1153 and within clasts consisting of quartz. The zircon shapes vary from rounded (1:1

aspect ratio) to more elongate (1:5 aspect ratio)(Figure 11a) with irregular shapes also

occurring (Figure 11c). Some zircon grains were also cracked (Figure 11d) and visibly

altered by chlorite (Figure 11b). As deduced from SEM-MLA mapping, the zircons in

the samples are over 80% associated with chlorite and quartz at 46% and 36%

respectively.
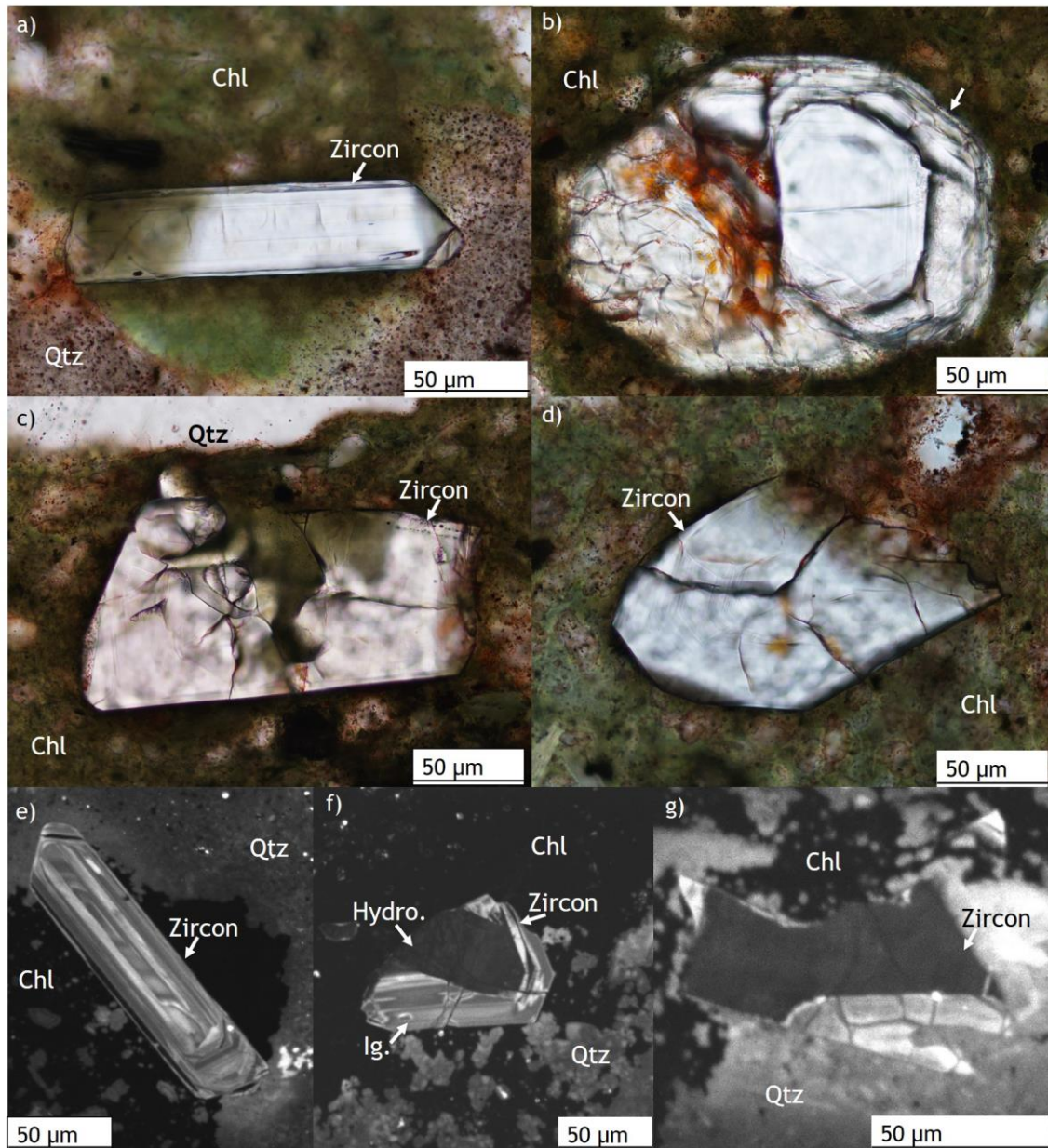
Figure 11 (a) Elongate zircon crystal in hematite stained quartz (TL), (b) Rounded quartz grain cracked and altered by chlorite (TL), (c) Zircon grain of an irregular shape (TL), (d) Zircon grains within chlorite matrix (TL), (e) CL image of elongate zircon crystal from image 11a with oscillating composition, (f) CL of zircon grain with domains of compositional zoning and a lack of zoning, (g) zircon clast with no compositional zoning. TL = Transmitted light, CL = Cathodoluminescence.

4.3.2 ZIRCON SEM – CL

The cathodoluminescence was used to image the compositional variation of the zircon grains to determine the zircon type (sedimentary, metamorphic or igneous) and aid LA-ICP-MS targeting. Zircon grains from samples 1083C and 860 were imaged.

Three different types of zircon grains were observed under CL. (1) Zircons with compositional zonation. (2) Zircons with a lack of oscillating zonation (Figure 11g). (3) Zircons that demonstrate having different areas containing oscillating patterns and also an area lacking in zonation (Figure 11f).

4.3.3 ZIRCON GEOCHEMSITRY

In this study the concordant zircons analyses have REE trends with a negative Eu anomaly and a positive Ce anomaly (Figure 12a). The zircon analyses of samples 860 and 1083C with an igneous REE pattern are also coincidental with oscillating zoning patterns observed under CL. The discordant data is more enriched in LREE overall and does not have Ce or Eu anomalies (Figure 12a). The slightly discordant analyses REE trends lie between that of the concordant and discordant data in terms of concentration (Figure 12a) with less distinctive Ce positive and Eu negative anomalies than the concordant data. The discordance of the zircon analyses roughly positively correlates to the LREE content (Figure 12b).

The Th/U ratio is used with the geochronology data to distinguish the different ages and compositions of zircons as suggested by Rubatto (2002). In the geochronological data two groups have been identified with a lower Th/U group corresponding to the older

population of data and the higher Th/U group corresponds to a younger zircon
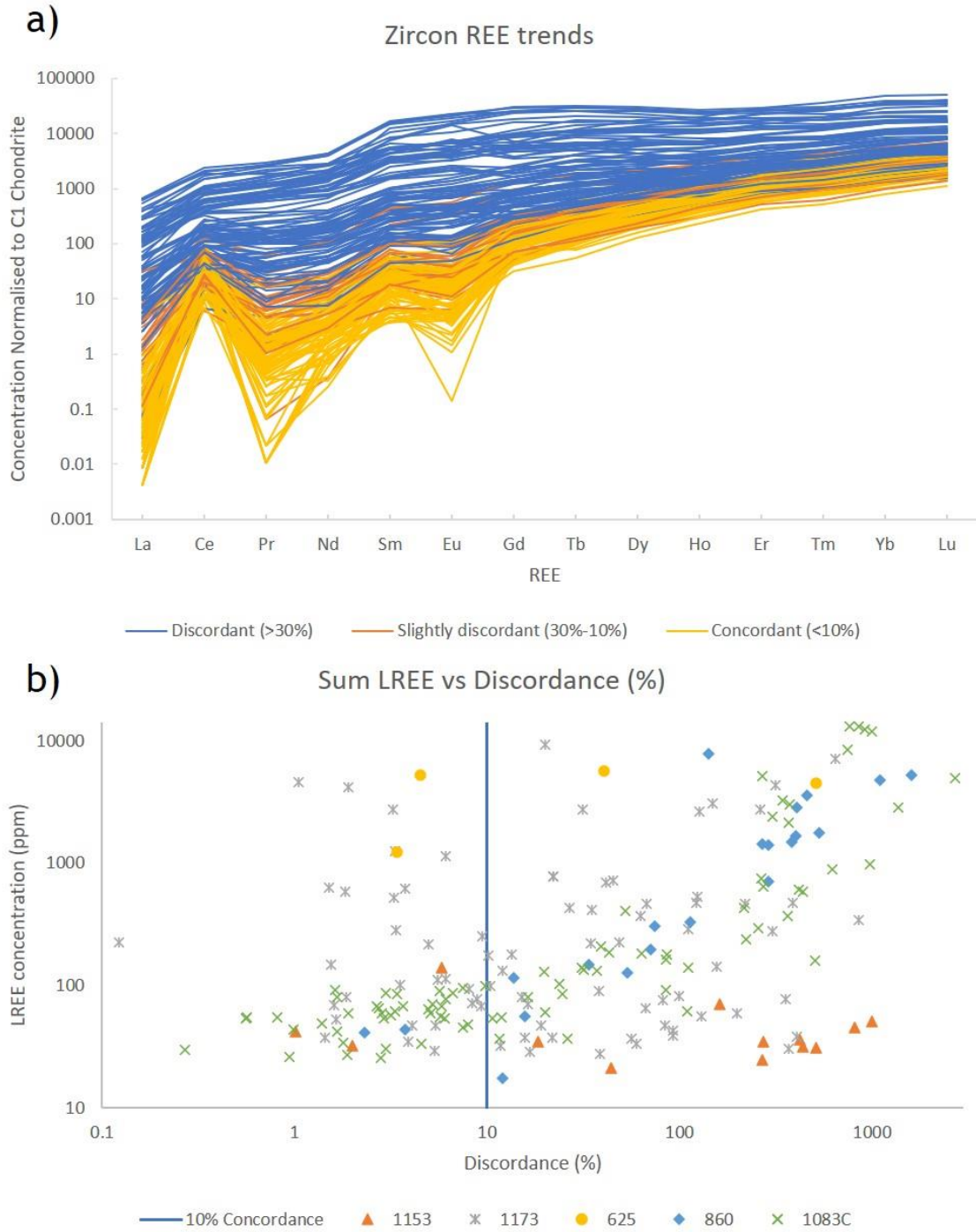
population (Figure 13).

Figure 12 (a) REE trends of zircon analyses grouped by % discordance (b) Discordance (%) vs sum of LREE of zircon analysis.

4.3.4 ZIRCON GEOCHRONOLOGY

Two hundred and twenty-nine analyses were collected on 98 zircon grains across 5 samples which resulted in 200 compositionally acceptable analyses. The composition criteria for the zircon analysis revealed a group of zircons with high aluminium content that were not included for age calculations. The resulting uranium and lead isotope concentrations, calculated ratios and associated errors along with the corrected age and 2σ propagated errors of each zircon analysis are included in Appendix C. All samples have observable lead loss trending back to approximately present day (Figure 13).

Sample 1083C consists of eighty-two analyses with an upper intercept of 1884 ± 33 Ma (MSWD=0.24, n=9) for the lower Th/U ratio zircons and 1636 ± 19 Ma (MSWD=0.3, n=29) for the higher Th/U ratio zircons when anchored at 0 Ma (Figure 13a). The corresponding weighted mean $^{207}Pb/^{206}Pb$ ages of the concordant analyses are 1868 ± 15 Ma (MSWD=0.2, n=9) and 1616 ± 11 Ma (MSWD=0.29, n=28) respectively (Figure 13a).

Sample 860 is a granite breccia and contains only a lower Th/U concordant group with twenty-one analyses (Figure 13b). There are two concordant analyses with a weighted mean $^{207}Pb/^{206}Pb$ age of 1843 ± 214 Ma (MSWD=0.3). The whole data set intercepts concordia at 1791 ± 56 Ma when anchored at 0 Ma (MSWD=8.2, n=21) (Figure 13b).

Sample 1173 resulted in eighty analyses with an upper intercept of 1630 ± 18 Ma (MSWD=1.1, n=20) and 1912 ± 51 Ma (MSWD=0.25, n=5) for the higher and lower Th/U grouped zircons respectively (Figure 13c). The correlating weighted mean

^{207}Pb/^{206}Pb age of the concordant higher and lower Th/U ratio groups are 1621 ± 19 Ma (MSWD=1.01, n=20) and 1904 ± 27 Ma (MSWD=0.27, n=5) (Figure 13c).

Sample 1153 has thirteen analyses, three of which were concordant analyses with ^{207}Pb/^{206}Pb ages of 1854±49 Ma, 1607±92 Ma and 1581±106 Ma (Figure 13d).

Sample 625 resulted in two concordant analyses has a weighted mean ^{207}Pb/^{206}Pb age of 1634 ± 259 Ma (MSWD=0.26). The four analyses have an upper intercept 1779 ± 5 (MSWD=43) when anchored at 0 Ma (Figure 13e).
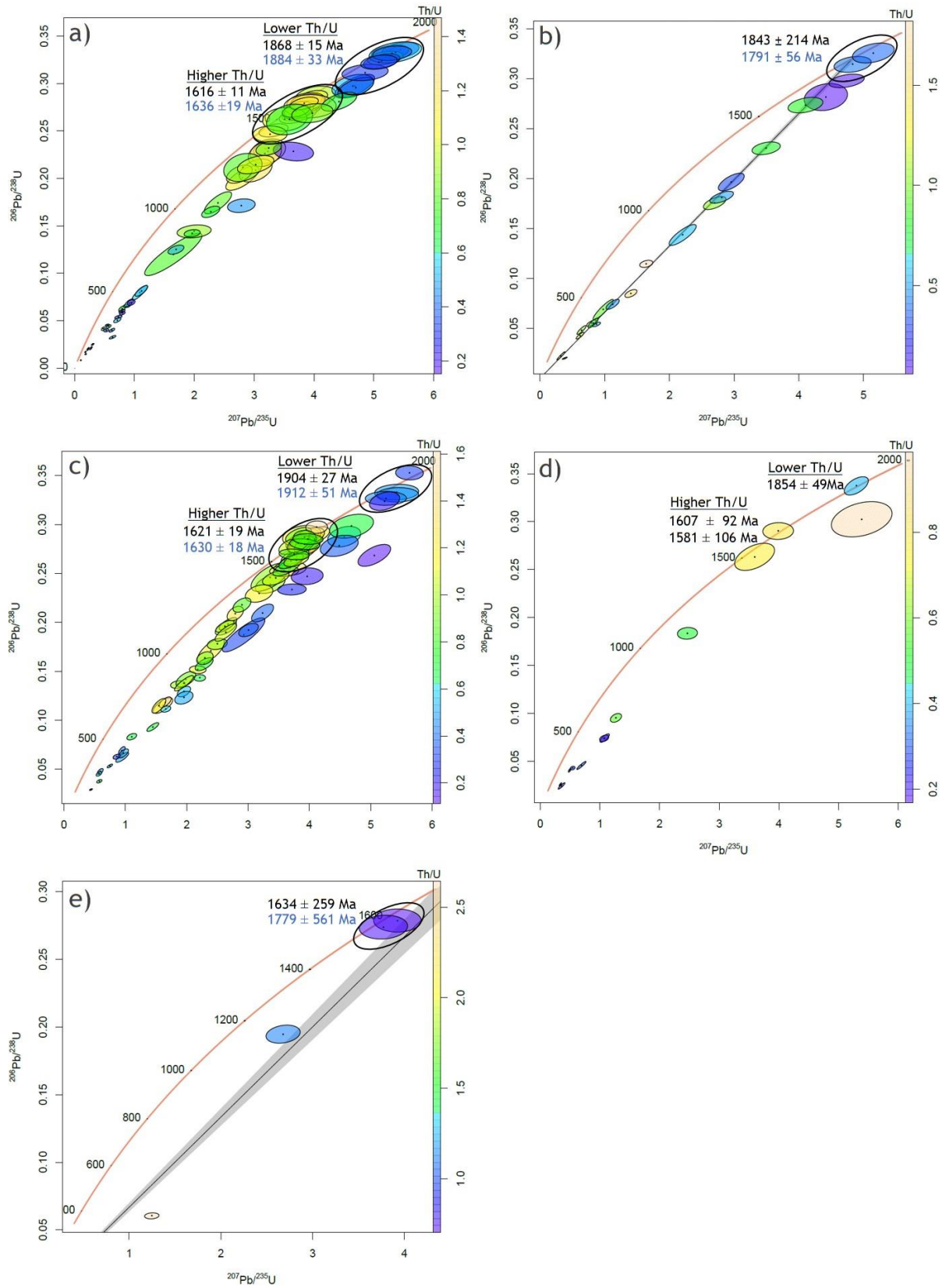
Figure 13 - Concordia plots of zircon analyses from sample (a) 1083C, (b) 860, (c) 1173, (d) 1153, (e) 625. Ages coloured black represent ^{207}Pb/^{206}Pb weighted mean age and blue represents upper intercept concordia age. Errors quoted are 95% confidence interval with overdispersion.

4.4.1 MONAZITE GEOCHEMISTRY AND U-PB GEOCHRONOLOGY

4.4.2 MOANZITE MINERARLOGY

Monazite is observed within sample 1173 and 1083C as inclusions within quartz grains (Figure 14a, 14b and 14e) . They are rounded in shape and usually are 5-25 µm in size. Larger monazites of over 10 µm occur in the hematite altered matrix of mineralised sample 1153. Monazite has not been observed with bornite or chalcopyrite but occurs in close proximity (Figure 14c and 14d). The monazites of sample 1153 are also irregularly shape (Figure 14d).

Figure 14 (a) Monazite inclusion in quartz grain of sample 1083C as imaged by MLA, (b) Monazite inclusion in (a) imaged by Transmitted light (TL), (c) Monazite cluster in chlorite located adjacent to bornite of sample 1153 as ima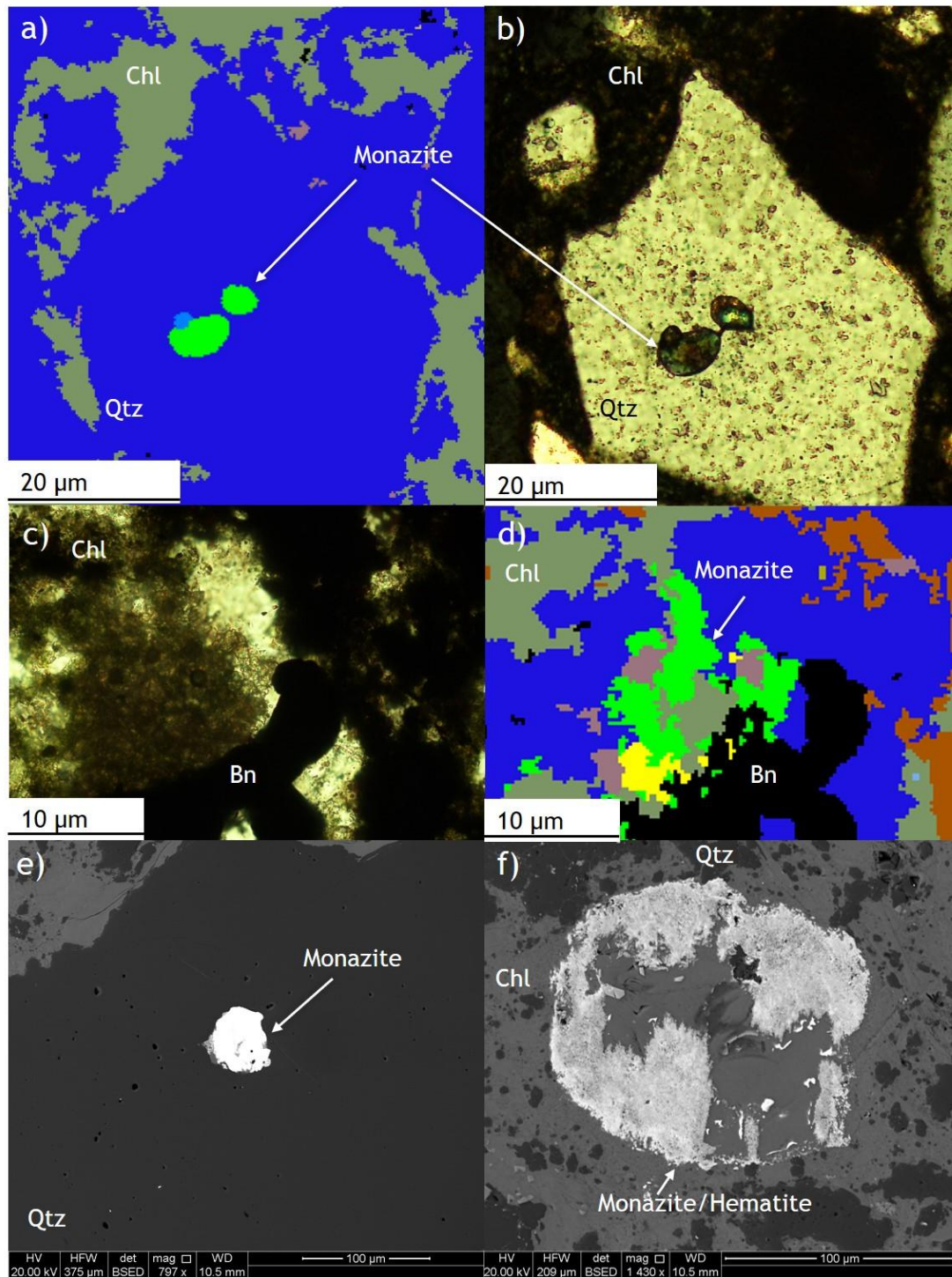ged by TL, (d) Monazite cluster in (c) imaged by MLA, (e) monazite inclusion in quartz imaged by SEM, (f) Mixed spectra of monazite and hematite (SEM).

As deduced by MLA mapping, monazite has an association with quartz (19%) and chlorite (56%) of over 70% respectively. The remainder of the mineral associations for monazite is hematite at 8.5% and biotite at 5.5% association. Monazite is most abundant in sample 1153 at 0.06% with over 5000 grains of mostly sub-micron size (refer to Appendix B).

Also identified from SEM-MLA a common mixed spectra exists between monazite and hematite (Figure 14f, Appendix B). This mixed spectra has similar associations but occurs in contact with chalcopyrite and pyrite at 2.3 and 0.5% association respectively.

4.4.2 MONAZITE GEOCHEMISTRY

Two groups of monazites have been identified from the trace element data of samples 1153, 1173 and 1083C (Figure 15a); (1) monazites with a negative Eu anomaly, relatively enriched in HREE and Th content of over 5 wt % and (2) monazites without a negative Eu anomaly, less enriched in HREE and a Th content under 2 wt% (Figure 15a).

4.4.3 MONAZITE GEOCHRONOLOGY

The resulting uranium and lead isotope concentrations, calculated ratios and associated errors along with the corrected age and 2σ propagated errors of each monazite analysis are included in Appendix C.

One hundred and sixty-five monazite analyses were obtained from samples 1153, 1173 and 1083C resulting in 83 clean analyses. The data was filtered for compositional integrity against various compositional criteria for monazite which determined the

analyses used for U-Pb geochronology. The data left out from age calculations are grouped as contaminants of Fe and Cu, low phosphorus and a various contaminants group (Appendix C). The monazites have been presented as non-mineralised and mineralised samples.

Samples 1083C and 1173 are both unmineralized in which contains both groups of monazites of higher and lower Th content (15b). The concordant analyses are all of a higher Th content, have Eu anomalies and occur as an inclusion in quartz clast. The concordant monazite analyses have a weighted mean $^{207}Pb/^{206}Pb$ age of 1848 ± 13 Ma (MSWD=1.72, n=16/18 rejected) (Figure 15b).

Sample 1153 is mineralised and contains only monazites of lower Th content and no Eu anomaly (Figure 15d). The data is scattered and the concordant data varies from 1200 Ma to 2100 Ma with a concentration from 1800-1500 Ma (Figure 15c and 15d). Overall the concordant monazite analyses from this sample have a weighted mean $^{207}Pb/^{206}Pb$ age of 1663 ± 80 Ma (MSWD=11.1, n=20) (Figure 15b).
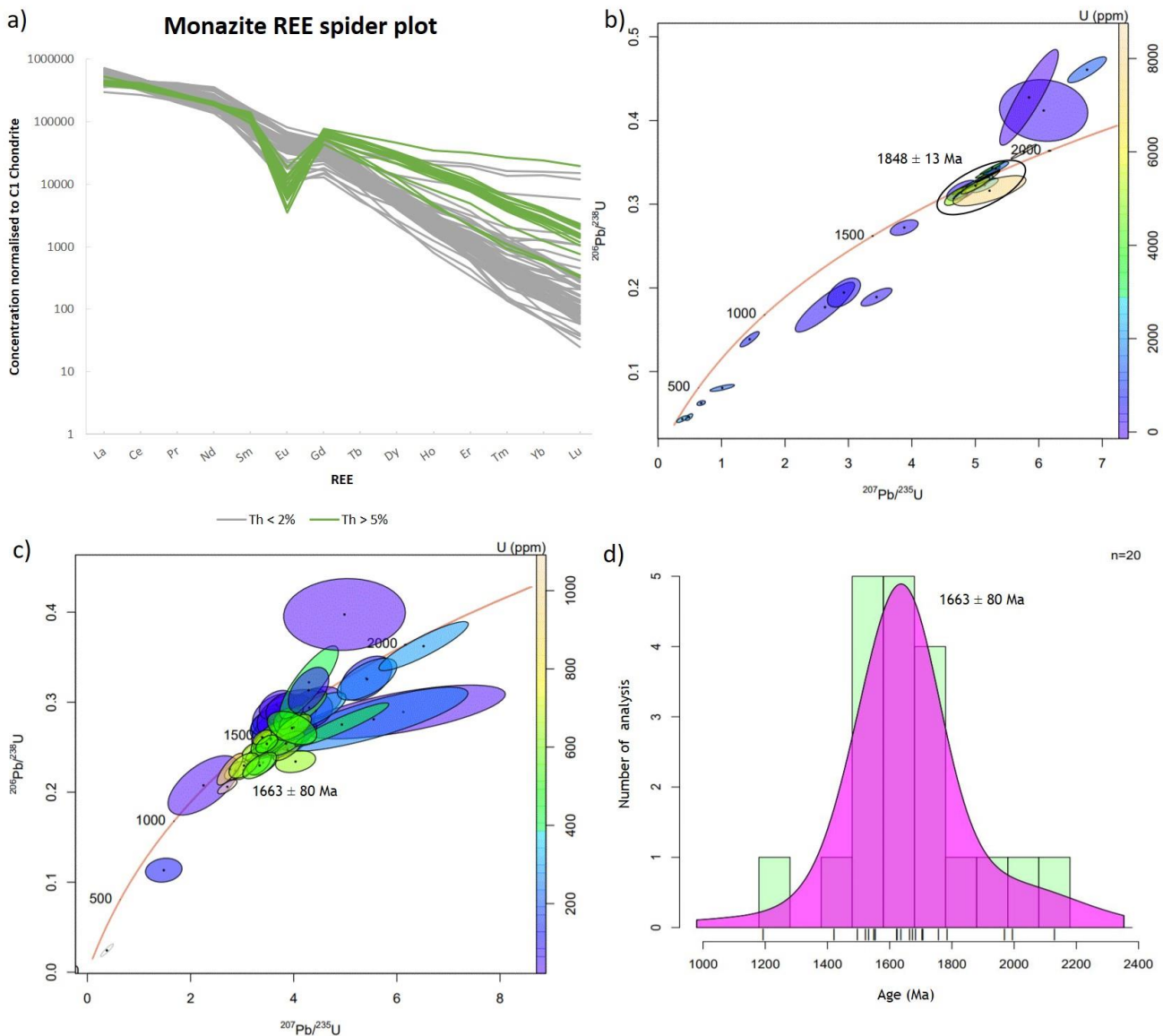
Figure 15 (a) Monazite REE spider plot of samples 1173, 1083C and 1153 coloured by Th content, (b) Concordia plot of monazite analyses from unmineralised samples 1173 and 1083C, (c) Concordia plot of monazite analyses from mineralised sample 1153, (d) KDE plot of concordant ages from sample 1153.Weighted mean $^{207}Pb/^{206}Pb$ ages on the Concordia plots are represented in black with 95% confidence interval error accounting for overdispersion.

4.5 RUTILE MINERALOGY

The rutile observed under thin section mostly occurs in the chlorite matrix or hematite stained quartz clasts and is either sub-euhedral in shape and 10-50 µm in size (Figure 16a) or elongate crystals up to 120 µm in length occurring in pockets (Figure 16b).

More irregular or altered crystal pockets do occur (Figure 16c) and one large grain up to

600 µm in size was identified from sample 1083C (Figure 16b).
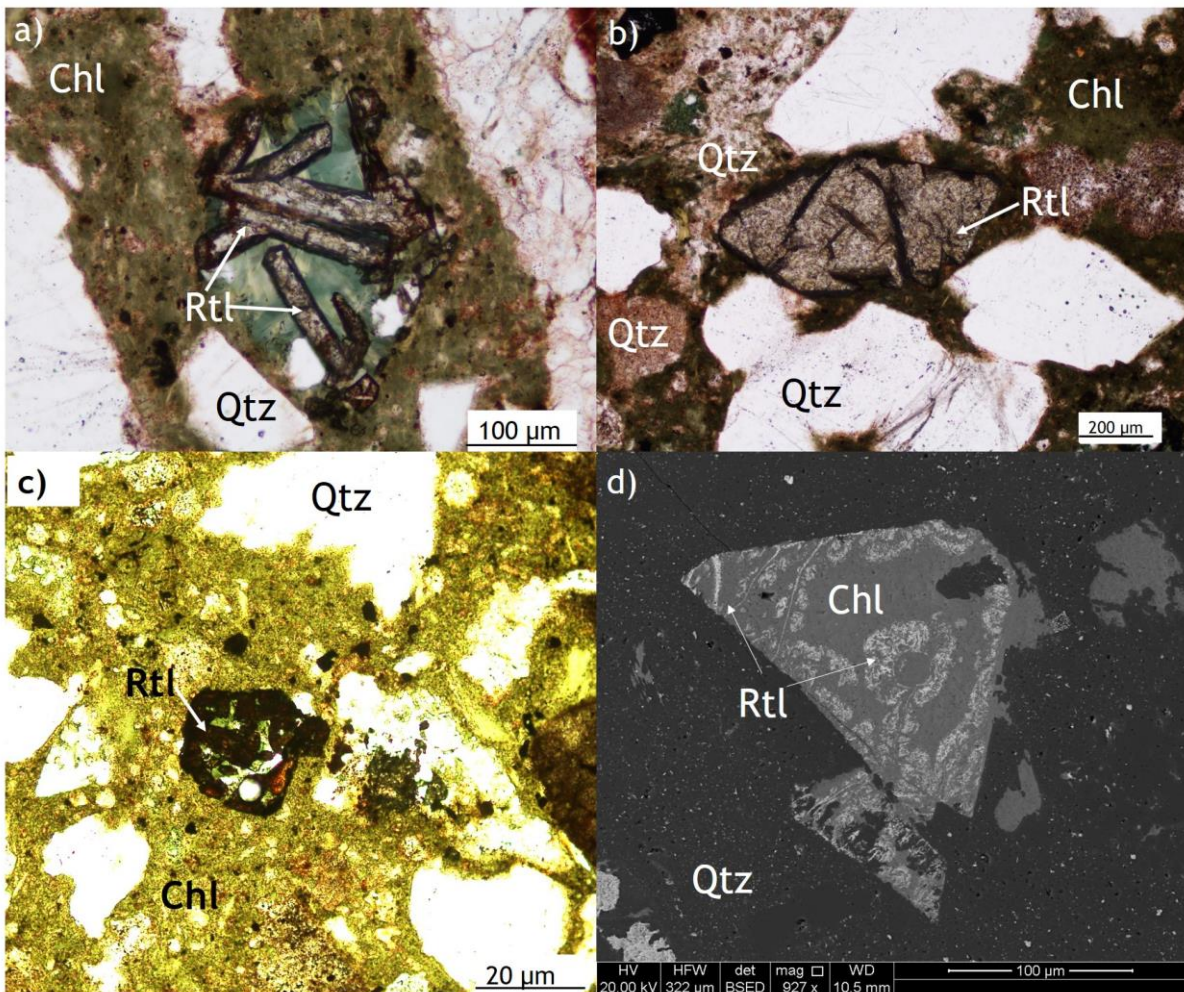
Figure 16 (a) Elongate rutile crystals in a pocket within chlorite (TL), (b) Sub-euhedral rutile grain of approximately 600 µm size (TL), (c) Rutile pocket with rounded and irregular shaped grains, (d) Very-fine rutile in chlorite grain (SEM).

As identified by MLA rutile also occurs as smaller grains ($< 1µm$) within chlorite and

quartz with ilmenite and rarely fine grains of REE-aluminate or brannerite. Rutile is

associated with 85% chlorite (60%) and quartz (25%), 2.3% ilmenite and 2.4% biotite.

Under SEM rutile was identified very-finely mixed with chlorite grains (Figure 16d)

and a separate spectra was created for MLA mapping.

4.5.2 Rutile Geochronology

The resulting uranium and lead isotope concentrations, calculated ratios and associated errors along with the corrected age and 2σ propagated errors of each rutile analysis are included in Appendix C.

Fifty-four analyses were completed on thirty-four rutile grains which were subsequently passed through various compositional criteria. Five analyses from two grains passed the compositional criteria (Figure 17a). Of the data that did not pass the criteria, four groups can be identified which correlate to high silica and thorium, high common lead and thorium, high ^{208}Pb compared to ^{238}U , and a complete outlier (Appendix C). The resulting lower age intercept of the age plot intercepted concordia at 1591 ± 84 Ma (Figure 17a). The two concordant analyses have a weighted mean ^{207}Pb/^{206}Pb age of 1771 ± 62 Ma (MSWD = 0.028).

4.5.3 Rutile Geochemistry

The five analyses have an average iron concentration of 86 ppm for grain 1 and 2697 ppm for grain 10 (Figure 17b). The Nb/Ta ratio of grain 1 is 20.5 and 5.8 for grain 10 (Figure 17b). Both grains sub-euhedral in shape which indicates they are not sedimentary.
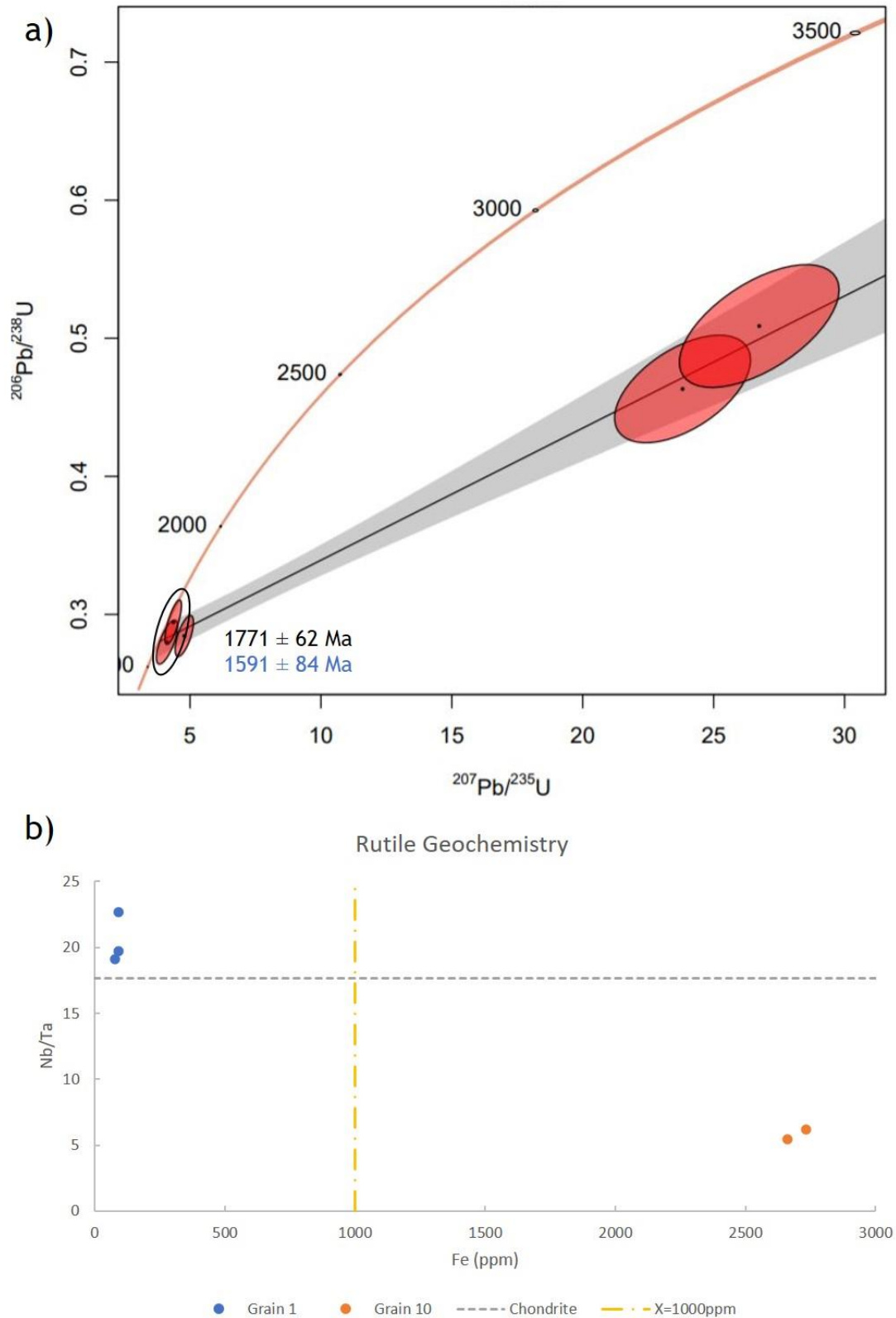
Figure 17 (a) Concordia plot of rutile analyses from sample 1083C with weighted mean $^{207}Pb/^{206}Pb$ age in black and upper intercept age in blue, (b) Rutile geochemistry of Fe content vs Nb/Ta ratio from sample 1083C.

5. DISCUSSION

The discussion has been divided into four sections corresponding to the four research questions as previously mentioned in the introduction. Each section will introduce the research question in italics and follow with a corresponding discussion to address the question.

What is the composition of the VSB?

In this study the VSB is mostly quartz and chlorite which range from 46%-70% and 21%-35% area respectively (excluding sample 625). The quartz is mostly angular clasts or can be contained in lithic, felsic or granite clasts. The chlorite makes up the fine matrix and chlorite altered clasts such as granite and ex-mafic clasts. Other clasts include hematite stained felsic clasts, metasediments and those associated with mineralisation. Mineralisation is carried by hematite which ranges from and includes sulphides; bornite, chalcopyrite and pyrite in samples 1153, 1083A and 1083B. The mineralised sample 1153 contains approximately 17.5% hematite and 1.8% chalcopyrite.

What is the age and origin of the VSB?

The concordant zircon analyses are interpreted as igneous as they have the REE trends of unaltered igneous zircon grains of a positive Ce anomaly, a negative Eu anomaly and enriched HREE compared to the LREE (Hoskin & Schaltegger, 2018). The concordant

zircon data of samples 1083Ca and 860 also corresponds to grains with oscillating composition also suggesting igneous province. The discordant analyses have a higher LREE content, flatter REE trend and correlate to an absence of oscillating composition when observed under CL. These zircon are interpreted as hydrothermal.

The two age populations of concordant igneous analyses vary in Th/U ratio. Zircon Th/U decreases with increasing SiO2 content of the whole rock and its Th/U due to magma partitioning of incompatible Th compared to U (Kirkland et al., 2015). This suggest the older population which has a lower Th/U ratio is from a higher SiO2 magma source than the younger population.

Of the samples that contained a lower Th/U group of zircon analyses all but sample 1173 fall within error of the ages of the Donington Granitic Suite between 1846 (Reid & Hand, 2008) and 1859 Ma as inferred and from U/Pb dating (Jagodzinski, 2005) . When all the samples with lower Th/U zircons are combined they result in a weighted mean ^{207}Pb/^{206}Pb age of 1872 ± 17 Ma which also lies within error of the Donington Suite.

The higher Th/U zircon analyses belong to felsic, quartz and chlorite grains as well as the matrix. Samples 1083C and 1173 have weighted means of 1616 ± 11 Ma and 1621 ± 19 Ma which reflects St Peter Suite age (1606 ± 6 to 1630 Ma (Jagodzinski & Reid 2016, Reid et al. 2017). A single pink felsic clast interpreted as rhyolite (Pontifex, 2012) from sample 1173 has over 16 zircon grains. The concordant analyses from this clast have a weighted average mean ^{207}Pb/^{206}Pb age of 1629 ± 29 Ma (MSWD=1.22, n=11) which corresponds to St Peter Suite age. Samples 625 and 1153 have large errors that

suggest either St. Peter Suite age or Gawler Range Volcanics (1595.5-1589 Ma;

Ferguson et al. 2019 & Fanning et al., 1988 in Skirrow, 2007). Over all the samples

with the higher Th/U zircons have a weighted mean $^{207}Pb/^{206}Pb$ age of 1619 ± 10 Ma

which correspond to the St Peter Suite age.

As two ages are observed in this rock, the relationship between the populations suggest

the rocks were either deposited together or one was relatively moved to the location of

the other. Due to the consistency in ages observed in the zircons analysed it suggests

these ages are likely not detrital, but directly reflect sources from known igneous suites.
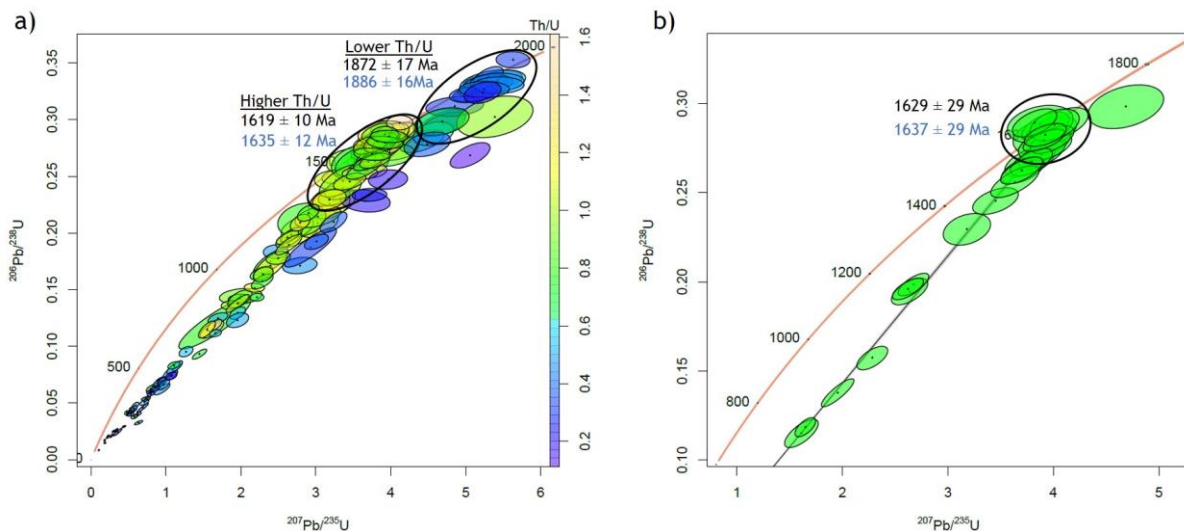
Figure 18 (a) Concordia plot of zircons from samples 1083C, 1153, 1173 and 625, (b) Concordia plot of hemaite stained porphyry clast. The weighted mean $^{207}Pb/^{206}Pb$ ages are denoted in black and the upper intercept ages are denoted in blue.

Two types of monazites are observed; igneous and hydrothermal. Igneous monazites

have a ThO2 content of 3 to >5 wt% (2.6->4.4 wt% Th) with hydrothermal monazites

usually having a lower ThO_2 content of 0-1 wt% (0-0.9 wt% Th) (Schandl and Gorton,

2004). The group of monazites with an Eu anomaly, high Th content and occurrence as

inclusions in quartz is consistent with an igneous origin. The remaining monazites are

hydrothermal as consistent with three major characteristics; (1) Occur as clusters of grains in a small area or euhedral in shape, (2) Occurs in contact with copper oxides or sulphides and (3) relatively depleted in ThO_2 (Schandl and Gorton, 2004).

The igneous monazites from non-mineralised samples have a weighted $^{207}Pb/^{206}Pb$ age of 1848 ± 13 Ma which correlates with the Donington Suite age (~1855 Ma).The hydrothermal monazites of the mineralised sample 1153 have a range of concordant ages from approximately 2100-1200 Ma. The concordant monazite analyses concentrate around 1800-1500 Ma with a weighted mean $^{207}Pb/^{206}Pb$ age of 1663 ± 80 Ma (MSWD = 11.1).

The range of concordant monazite ages could represent multiple events observed across the Gawler Craton as occurring from 2100 Ma to 1200 Ma. This includes monazite dated for mineralisation at Oak Dam (1455 ± 20 Ma; Davidson et al., 2007), zircon resetting (1690 Ma; Jagodzinski, 2014) and zircons aged at 1700 Ma incorporated in the polymictic conglomerate (Cherry et al., 2018) and younger ages such as the break-up of Rodinina (1100-1300 Ma; Condie, 2005). Other possible related ages explored in this study relate to the GRV (1589-1595.5 Ma; Ferguson et al. 2019), St. Peter Suite (1607 ± 6 to 1630 Ma; Jagodzinski & Reid 2016) and Donington Suite (1846-1859 Ma;Reid & Hand, 2008; Jagodonski, 2005). Concluding this, these monazites concordant ages suggest multiple generations of mineralisation and/or hydrothermal events.

Most metamorphic rutile has an iron content of over 1000 ppm Fe (Zack et al., 2004a) and hydrothermal rutile can contain more than 5000 ppm Fe (Müller and Halls, 2005).

Subchondritc Nb/Ta is associated with continental crust, volcanic island arc and most island arc basalts (Meinhold, 2010). Suprachondritic Nb/Ta is associated with metasomatized lithoshpheric mantle and continental lithospheric mantle (Kalfourn et al., 2002). Euhedral and needle-like grains suggest a metamorphic origin over detrital (Banfield and Veblen, 1991) but primary igneous rutile can also rarely occur as euhedral grains (Carruzzo et al., 2006). Grain 1 does not reflect an iron content of hydrothermal or metamorphic rutile and has a euhedral shape and therefore is suggested here as an igneous rutile. Grain 10 reflects an iron content of hydrothermal or metamorphic rutile. The rutile analyses intercepted concordia at 1591 ± 84 Ma which is roughly the age of copper-gold mineralisation around the Gawler Craton (Skirrow, 2002). Due to the low precision of rutile age deduced, this age could be associated with a variety of events.

The incorporation of the Donington Granite host into the VSB is interpreted as local and syngenetic with the other clasts within the VSB. This is due to the granite being subsequently brecciated during formation of the complex, erosion from the surface at the unconformity and the lack of consistent sorting (well sorted to unsorted) of the different type of clasts within the VSB. The volcanic sediments within the VSB are well rounded and therefore interpreted as having travelled to the site of the breccia complex. This includes the felsic and mafic clasts although should be subject to further investigation. The angular quartz clasts and lithic fragments are likely from a more local source as the shape infers the clasts did not travel far. The previous theories for the origin of the VSB (Sawyer, 2014 and Taylor, 2014) have little evidence and fail to explain the incorporation of the angular quartz within the conglomerate.

The Olympic Dam deposit (Figure 1) has a polymictic volcanic clastic conglomerate containing GRV with zircon ages from LA-ICP-MS of 1603.7 ± 19.6 Ma and CA-TIMS age for felsic clasts of 1594.73 ± 0.30 Ma with mafic clasts inferred at ca 1590 Ma (Figure 19; Cherry et al. 2018). The deposition of the conglomerate occurred after the emplacement of the GRV upon the Roxby Down Granite (RDG; Cherry et al., 2018). NE to NW faults propagated causing subsidence at the deposit site which allowed the conglomerate unit to deposit (Cherry et al., 2018 and McPhie et al., 2016). Further erosion and faulting incorporated the host RDG into the deposit and the Pandurra Formation was then unconformably deposited (Cherry et al., 2018; Cherry et al., 2017), subsequently eroded and the Neoproterozoic sediments were overlain (Cherry et al., 2018).

Similar environments are observed at Carrapateena with NE and NW trending faults identified as active during the associated Hiltaba deformation event (Murphy et al., 2012). This could have caused regional subsidence over the CBC creating a basin for the sediments to accumulate as speculated at OD (McPhie et al. 2016). The younger population of higher Th/U zircons of a $^{207}Pb/^{206}Pb$ age of 1619 ± 10 Ma does lie within error of that found for the polymictic conglomerate at Olympic Dam of 1603.7 ± 19.6 Ma (Figure 19; Cherry et al., 2018). If these units are correlated the clast sizes suggest high energy event extended from Olympic Dam and over Carrapateena and could be correlated as far as Roopena (Figure 1) where another similar unit has been identified to carry both St. Peter Suite and minor GRV clasts (Curtis et al., 2016).

The deposition event of the VSB which is also considered a conglomerate is constrained to the youngest zircon clast with a mean of 1580 Ma. The minimum age of deposition is constrained to the age of the Neoproterozoic cover at approximately 650 Ma but could be suggested as occurring with the inferred presence of the of the regional Panadura formation unconformably overlying the CBC before being subsequently eroded. As the VSB is observed with mineralisation it must be pre or syn deposition which could further constrain the deposition age. Mineralisation is currently dated as occurring after the Re-Os date from pyrite of 1598 ± 6 Ma (Williams, 2014) but may provide a constraint in the future with improved techniques.
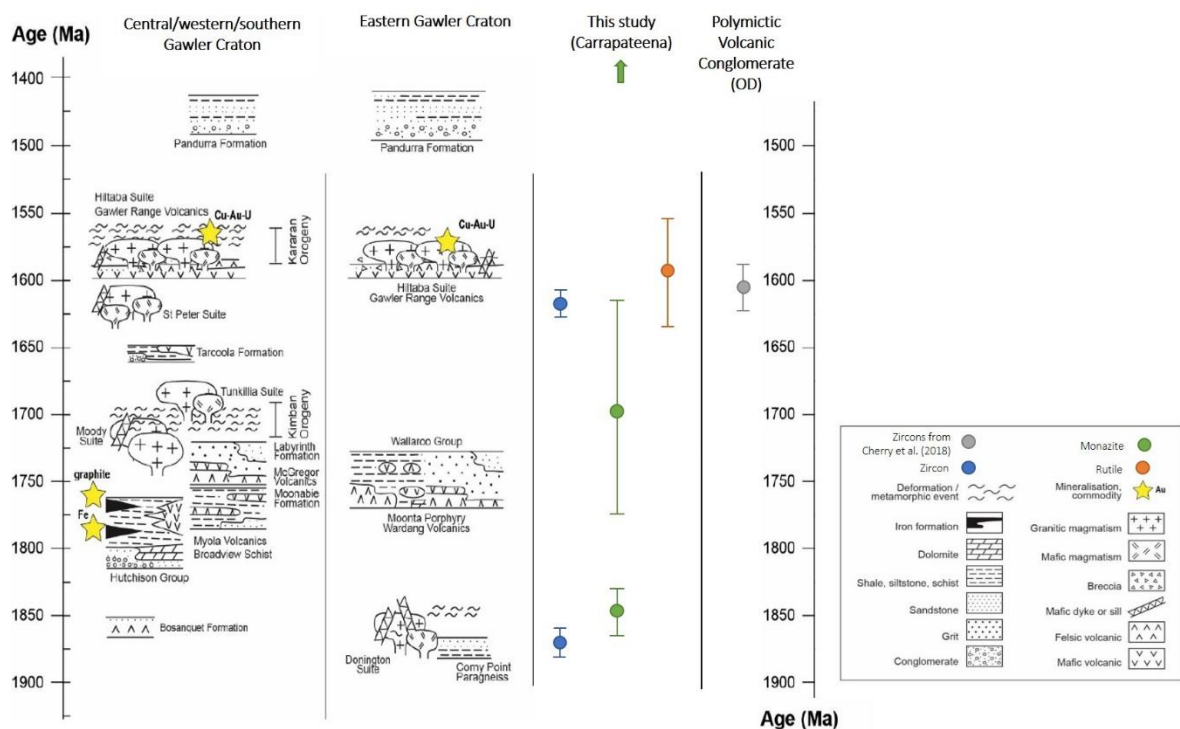

Figure 19 - Simplified space-time diagram illustrating main lithospheric elements of the Gawler Craton (Reid, 2019) with weighted mean $^{207}Pb/^{206}Pb$ Pb ages from this study and zircons from the polymictic volcanic conglomerate at Olympic Dam (Cherry et al., 2018).

What was the tectonic setting at the time of the formation of the Sedimentary Volcanic Conglomerate and the resultant brecciation?

The proposed deposition of the VSB was deposited between 1580-650 Ma. Three tectonic events are suggested to occur in the Galwer Craton from 1575-1450 Ma (Hand et al, 2007). This includes the deformation associated with the Hiltaba suite (1595-1575 Ma), Kararan Orogeny (1570-1540 Ma) and Coorabie Orogeny (1470-1450 Ma). The Hiltaba suite associated deformation was the most extensive of events, spanning the entire craton compared the Kararan and Coorabie orogenies which occurred over the north and western parts of the craton (Hand et al., 2007). Very little records are observed for the Gawler Craton between the late Karanan orogeny and the deposition of the Stuart Shelf sediments. The only evidence observed over the CBC for the events mentioned above occurs during the deformation associated with the emplacement of the Hiltaba Suite (Murphy et al., 2012). As mentioned previously, a similar rock unit is the result of similar timed deformation in the form of NE and NW trending faults observed at Olympic Dam (McPhie et al., 2016; Cherry et al., 2018).

Can the Sedimentary Volcanic Conglomerate breccia host ore and/or REE minerals and if so does it contain the same ore an REE mineralogy as the main ore breccia?

Three copper minerals; bornite, chalcopyrite and chalcanthite also sulphide, pyrite, were found associated within the mineralised samples in thin section (Figure 7e, 7f and 8c). Bornite and chalcopyrite are the same copper minerals which dominate the bornite and

chalcopyrite zones within the deposit (Figure 4). The VSB as the CSBX and HSBX has elevated copper when compared to the barren zone and granite. The HSBX has a similar copper content to the main copper hosting breccia (Figure 10). Since the VSB has been subject to the hematite alteration that carries mineralisation, it's deposition is pre-mineralisation or syn-mineralisation.

REE minerals hosted in VSB as deduced by MLA include a Ce-Silicate and REE-aluminate (Appendix B) and monazite, xenotime and apatite. Monazites occur of the highest abundance in sample 1153 which contains copper mineral, bornite. It could be suggested that monazites are associated with the bornite due to the relative abundance when compared to the samples containing chalcopyrite and the non-mineralised samples. The Ce-Silicate, REE-aluminate and apatite all occur within the mineralised and non-mineralised samples. Xenotime occurs in higher abundances within the mineralised thin sections and hence can be associated with mineralisation. Xenotime, apatite and monazite all occur within the main ore breccia as determined by North et al. (2020). Ce-silicate and REE-aluminate however were not observed in main ore breccia (North et al., 2020). This may indicate different REE mineralogy is present in the VSB compared to the main ore but would require the analysis of more samples. Overall the REE content of the VSB as CSBX and HSBX variants is elevated when compared to granite (Figure 10). The HSBX has a similar mean REE content of the main copper breccia and barren hematite zone (Figure 10). Therefore the VSB could be considered a host of mineralisation and REE.

6. CONCLUSIONS

The Volcanic Sedimentary Breccia Unit (VSB) is mostly composed of quartz and chlorite at over 64% area of the samples analysed. The clasts consist of angular quartz, volcanic (felsic and mafic) clasts, granite and lithic clasts. The matrix consists of fine chlorite and comminuted conglomerate clasts.

A higher U/Th concordant zircon group has a weighted mean $^{207}Pb/^{206}Pb$ of 1619 ± 10 Ma age which corresponds to St Peter Suite age. The lower concordant U/Th zircon group are interpreted as belonging to the Donington suite granite (1855 Ma; Jagodinzinski, 2005). Igneous monazites of samples 1083C and 1173 have a $^{207}Pb/^{206}Pb$ age of 1848 ± 13 Ma which also correlates to the Donington suite granite. Hydrothermal monazites associated with mineralisation have a range of concordant ages spanning 2100 Ma to 1200 Ma, with a group of monazites with a weighted $^{207}Pb/^{206}Pb$ age of 1663 ± 80 Ma , which is suggested to reflect multiple events. Five rutile analyses resulted in a lower intercept of 1591 ± 84 Ma which corresponds roughly to mineralisation in the Gawler Craton.

The origin of the VSB is suggested to have occurred as the result of tectonic movement along NW and NE trending Hiltaba aged faults which have created void space for deposition of detrital material. It is proposed the VSB was deposited somewhere between 1580-1440 Ma, which is the range between the youngest clast grain identified in this study and the suggested deposition age of the overlying Pandurra formation. However, a lack of evidence for the Panadura formation overlying the formation restricts the actual constraints of deposition to 1580-650 Ma.

7. ACKNOWLEDGMENTS

8. REFERENCES

Banfield, J. F., Veblen, D. R., & Smith, D. J. (1991). The identification of naturally occurring TiO2 (B) by structure determination using high-resolution electron microscopy, image simulation, and distance-least-squares refinement. *American Mineralogist, 76*(3-4), 343-353.

Barry Murphy, P. B., Charles Funk. (2012). *Interpretation of gravity and aeromagnetic data over the Carrapateena region, South Australia, and exploration targeting* [Internal Report].

Betts, P. G., Giles, D., Foden, J., Schaefer, B. F., Mark, G., Pankhurst, M. J., Forbes, C. J., Williams, H. A., Chalmers, N. C., & Hills, Q. (2009). Mesoproterozoic plume-modified orogenesis in eastern Precambrian Australia. *Tectonics, 28*(3).

Bull, S., & Meffre, S., (2013, March). *Detrital zircon geochronology of the Adelaidean at Carrapateena.* OZ Minerals [Internal Report].

Bull, S., & Meffre, S., (2012, June). *Carrapateena Geochronology.* OZ Minerals [Internal Report].

Carruzzo, S., Clarke, D. B., Pelrine, K. M., & MacDonald, M. A. (2006). Texture, composition, and origin of rutile in the South Mountain Batholith, Nova Scotia. *The Canadian Mineralogist, 44*(3), 715-729.

Cherry, A. R., Ehrig, K., Kamenetsky, V. S., McPhie, J., Crowley, J. L., & Kamenetsky, M. B. (2018). Precise geochronological constraints on the origin, setting and incorporation of ca. 1.59 Ga surficial facies into the Olympic Dam Breccia Complex, South Australia. *Precambrian Research, 315*, 162-178.

Cherry, A. R., McPhie, J., Kamenetsky, V. S., Ehrig, K., Keeling, J. L., Kamenetsky, M. B., Meffre, S., & Apukhtina, O. B. (2017). Linking Olympic Dam and the Cariewerloo Basin: Was a sedimentary basin involved in formation of the world's largest uranium deposit? *Precambrian Research, 300*, 168-180.

Condie, K.C., (2005). Earth as a an Evolving Planetary System; *The Supercontinent Cycle and Mantle-Plume Events:* Academic Press

Curtis, S., Wade, C., & Reid, A. (2018). Sedimentary basin formation associated with a silicic large igneous province: stratigraphy and provenance of the Mesoproterozoic Roopena Basin, Gawler Range Volcanics. *Australian Journal of Earth Sciences, 65*(4), 447-463.

Daly, S. (1998). Tectonic evolution and exploration potential of the Gawler Craton, South Australia. *AGSO J. Aust. Geol. Geophys., 17*, 145-168.

Davidson, G. J., Paterson, H., Meffre, S., & Berry, R. F. (2007). Characteristics and origin of the Oak Dam East breccia-hosted, iron oxide Cu-U-(Au) deposit: Olympic Dam region, Gawler craton, South Australia. *Economic Geology, 102*(8), 1471-1498.

Fanning, C., Flint, R., Parker, A., Ludwig, K., & Blissett, A. (1988). Refined Proterozoic evolution of the Gawler craton, South Australia, through U-Pb zircon geochronology. *Precambrian Research, 40*, 363-386.

Fanning, C., Teale, G., & Reid, A. (2007). *A geochronological framework for the Gawler Craton, South Australia*. Primary Industries and Resources SA.

Ferris, G. M., Schwarz, M. P., & Heithersay, P. (2002). The geological framework, distribution and controls of Fe-oxide Cu-Au mineralisation in the Gawler Craton, South Australia. Part I– Geological and tectonic framework. *Hydrothermal iron oxide copper-gold and related deposits: A global perspective, 2*, 9-31.

Giles, C. (1988). Petrogenesis of the Proterozoic Gawler Range Volcanics, South Australia. *Precambrian Research, 40*, 407-427.

Hand, M., Reid, A., & Jagodzinski, L. (2007). Tectonic framework and evolution of the Gawler Craton, Southern Australia. *Economic Geology, 102*(8), 1377-1395.

Hoskin, P.W.O., & Schaltaltegger, U.,(2018). Zircon; *The Composition of Zircon and Igneous and Metamorphic Petrogenesis:* De Gruyter, Inc.

Jagodzinski, E. (2005). Compilation of SHRIMP U-Pb geochronological data, Olympic Domain, Gawler Craton, South Australia, 2001-2003. *Geoscience Australia Record, 20*, 197.

Jagodzinski, E. (2014). The age of magmatic and hydrothermal zircon at Olympic Dam. Australian Earth Sciences Convention (AESC), Sustainable Australia,

Jagodzinski, E., Hand, M., & Reid, A. (2012). *SHRIMP U-Pb Geochronology of Archaen to Palaeoproterozoic Rocks from the Southern Eyre Peninsula*. Department for Manufacturing, Innovation, Trade, Resources and Energy.

Jagodzinski, E., Reid, A., Crowley, J., McAvaney, S., & Wade, C. (2016). Precise Zircon U-Pb Dating of a Mesoproterozoic Silicic Large Igneous Province: The Gawler Range Volcanics and Benagerie Volcanic Suite, South Australia. South Australia, Australian Earth Sciences Convention,

Jagodzinski, E. A., & Reid, A. (2016). *U-Pb geochronological data from drill holes Nundroo 3 DDH and Nundroo 2 DDH, Fowler Domain, western Gawler Craton*. Department of State Development.

Kirkland, C., Smithies, R., Taylor, R., Evans, N., & McDonald, B. (2015). Zircon Th/U ratios in magmatic environs. *Lithos, 212*, 397-414.

Laughton, J. R. (2004). *The Proterozoic Slab volcanics of northern Yukon, Canada: megaclasts of a volcanic succession in Proterozoic Wernecke Breccia, and implications for the evolution of northwestern Laurentia* Theses (Dept. of Earth Sciences)/Simon Fraser University].

McPhie, J., Orth, K., Kamenetsky, V., Kamenetsky, M., & Ehrig, K. (2016). Characteristics, origin and significance of Mesoproterozoic bedded clastic facies at the Olympic Dam Cu–U–Au–Ag deposit, South Australia. *Precambrian Research, 276*, 85-100.

Meinhold, G. (2010). Rutile and its applications in earth sciences. *Earth-Science Reviews, 102*(1-2), 1-28.

Müller, A., & Halls, C. (2005). Rutile—the tin-tungsten host in the intrusive tourmaline breccia at Wheal Remfry, SW England. Mineral Deposit Research: Meeting the Global Challenge.

Murphy, B., Betts, P., & Funk, C., (2012, May). *Interpretation of Gravity and Aeromagentic Data over the Carrapateen Regoin, South Australia, and Exploration Targeting.* OZ Minerals [Internal Report].

Norris, A., & Danyushevsky, L. (2018). Towards Estimating the Complete Uncertainty Budget of Quantified Results Measured by LA-ICP-MS. *Goldschmidt: Boston, MA, USA*.

North, B., (2020). *The Geochemistry of Rare Earth Element-Bearing Minerals and their Relationship to Copper Sulphide Mineralisation at the Carrapateena Deposit, South Australia* [Unpublished honours thesis]. The University of Adelaide.

Pontifex, I.R., (2012). *Mineralogical Report No. 10124 – CAR050* (Report No.10124). OZ Minerals [Internal Report].

Reid, A. (2019). The Olympic Cu-Au Province, Gawler Craton: a review of the lithospheric architecture, geodynamic setting, alteration systems, cover successions and prospectivity. *Minerals, 9*(6), 371.

Reid, A., Jourdan, F., & Jagodzinski, E. (2017). Mesoproterozoic fluid events affecting Archean crust in the northern Olympic Cu–Au Province, Gawler Craton: insights from 40Ar/39Ar thermochronology. *Australian Journal of Earth Sciences, 64*(1), 103-119.

Reid, A., Pawley, M., Jagodzinski, E., & Dutch, R. (2016). Magmatic processes of the St Peter Suite, Gawler Craton: new U-Pb geochronological data and field observations. *Report book, 12*.

Reid, A. J., & Fabris, A. (2015). Influence of preexisting low metamorphic grade sedimentary successions on the distribution of iron oxide copper-gold mineralization in the Olympic Cu-Au Province, Gawler Craton. *Economic Geology, 110*(8), 2147-2157.

Reid, A. J., & Hand, M. (2012). Mesoarchean to mesoproterozoic evolution of the southern Gawler Craton, South Australia. *Episodes, 35*(1), 216-225.

Rubatto, D. (2002). Zircon trace element geochemistry: partitioning with garnet and the link between U–Pb ages and metamorphism. *Chemical geology, 184*(1-2), 123-138.

Ryan, C. G., Kirkham, R., Moorhead, G., Parry, D., Jensen, M., Faulks, A., Hogan, S., Dunn, P., Dodanwela, R., & Fisher, L. (2018). Maia Mapper: High definition XRF imaging in the lab. *Journal of Instrumentation, 13*(03), C03020.

Sawyer, M., (2014a). Geology of *Carrapateena: Geology, Alteration and Mineralisation of a major IOCG system.* OZ Minerals [Internal Report].

Sawyer, M., (2014b, March). *Carrapateena: Geology, Alteration and Mineralisation of a major IOCG system.* OZ Minerals [Internal Report].

Schandl, E. S., & Gorton, M. P. (2004). A textural and geochemical guide to the identification of hydrothermal monazite: criteria for selection of samples for dating epigenetic hydrothermal ore deposits. *Economic Geology, 99*(5), 1027-1035.

Skirrow, R., Bastrakov, E., Davidson, G., Raymond, O., & Heithersay, P. (2002). The geological framework, distribution and controls of Fe-oxide Cu-Au mineralisation in the Gawler Craton, South Australia. Part II-alteration and mineralisation.

Skirrow, R., Van Der Wielen, S., Champion, D., Czarnota, K., & Thiel, S. (2018). Lithospheric architecture and mantle metasomatism linked to iron oxide Cu-Au ore formation: Multidisciplinary evidence from the Olympic Dam Region, South Australia. *Geochemistry, Geophysics, Geosystems, 19*(8), 2673-2705.

Skirrow, R. G., Bastrakov, E. N., Barovich, K., Fraser, G. L., Creaser, R. A., Fanning, C. M., Raymond, O. L., & Davidson, G. J. (2007). Timing of iron oxide Cu-Au-(U) hydrothermal activity and Nd isotope constraints on metal sources in the Gawler craton, South Australia. *Economic Geology, 102*(8), 1441-1470.

Taylor, R., (2014). *20140505 Roger Taylor Carra Report.* OZ Minerals [Internal Report].

Tiddy, C. J., & Giles, D. (2020). Suprasubduction zone model for metal endowment at 1.60-1.57 Ga in eastern Australia. *Ore Geology Reviews*, 103483.

Vermeesch, P. (2018). IsoplotR: A free and open toolbox for geochronology. *Geoscience Frontiers, 9*(5), 1479-1493.

Wade, B., Barovich, K., Hand, M., Scrimgeour, I., & Close, D. (2006). Evidence for early Mesoproterozoic arc magmatism in the Musgrave Block, central Australia: implications for Proterozoic crustal growth and tectonic reconstructions of Australia. *The Journal of geology, 114*(1), 43-63.

Wade, C. E., Payne, J. L., Barovich, K. M., & Reid, A. J. (2019). Heterogeneity of the sub-continental lithospheric mantle and 'non-juvenile'mantle additions to a Proterozoic silicic large igneous province. *Lithos, 340*, 87-107.

Zack, T. v., Von Eynatten, H., & Kronz, A. (2004). Rutile geochemistry and its potential use in quantitative provenance studies. *Sedimentary Geology, 171*(1-4), 37-58.